Chemically driven carbon-nanotube-guided thermopower waves

Chemically Driven Carbon Nanotube-Guided Thermopower Waves

Wonjoon Choi [1,2], Seunghyun Hong [3], Joel T. Abrahamson [1], Jae-Hee Han [1], Changsik Song [1], Nitish Nair [1], Seunghyun Baik [3], Michael S. Strano [1*]

1 – Department of Chemical Engineering, Massachusetts Institute of Technology, Cambridge, MA, 02139, USA

2 – Department of Mechanical Engineering, Massachusetts Institute of Technology, Cambridge, MA, 02139, USA

3 – SKKU Advanced Institute of Nanotechnology, Department of Energy Science and School of Mechanical Engineering, Sungkyunkwan University, Gyeonggi, 440-746, Korea

*e-mail : strano@mit.edu

Correspondence should be addressed to M. S. S.

Theoretical calculations predict that by coupling an exothermic chemical reaction with a nanotube or nanowire possessing a high axial thermal conductivity, a self-propagating reactive wave can be driven along its length. Herein, such waves are realized using a 7-nm cyclotrimethylene-trinitramine annular shell around a multi-walled carbon nanotube and are amplified by more than 10^4 times the bulk value, propagating more than 2 m/s, with an effective thermal conductivity of 1.28 ± 0.2 kW/m/K at 2860 K. This wave produces a concomitant electrical pulse of disproportionately high specific power, as large as 7 kW/kg, that we identify as a thermopower wave. Thermally excited carriers flow in the direction of the propagating reaction with specific power that scales inversely with system size. The reaction also evolves an anisotropic pressure wave of high total impulse per mass (300 N-s/kg). Such waves of high power density may find uses as unique energy sources.

Introduction

The classical theory of heat conduction predicts that self-propagating chemical waves are possible when a non-linear source term, activated by temperature, is coupled to an exothermic reactive material that is also the heat conductor. The resulting wave velocity that radiates isotropically is known to vary exponentially with the inverse adiabatic reaction temperature [1], a fundamental material property. Such waves were first studied theoretically in 1938 by Zel'dovich and Frank-Kamenetskii [2], and experimentally verified for a wide range of technological applications, such as propulsion [3], chemical synthesis [4] and combustion [5]. The emergence of nanotube and nanowire systems, where phonons are quantum confined and scattering processes are minimized, has resulted in observations of axial thermal conductivity that are exceedingly high [6]. The properties of such systems are surprisingly invariant to mechanical deformation [7], even showing thermal rectification for anisotropically loaded specimens [8]. The question of how such systems support or modify a neighboring reaction wave has thus far been unexplored. It is known, for example, that only the thermal conductivity in the vicinity of the narrow reaction zone contributes to wave propagation [9]. If the phonon mean free path becomes commensurate with the length of this zone, a possibility for many one dimensional nanotube systems, an enormous acceleration of the reactive wave may result. In this work, we demonstrate the existence of such accelerated thermal waves and introduce a new phenomenon that results from their effect on carrier propagation, namely concomitant thermopower waves that yield a substantial specific power from a micro- or nano-scale source.

We verify the existence of such waves experimentally by creating both isolated and aligned arrays of multi-walled carbon nanotubes (MWNT) encased in a 7-nm-thick cyclotrimethylene-trinitramine

(TNA) annular coating (Fig. 1a). The synthesis procedure is based on a wet impregnation of a 90-mM TNA in acetonitrile solution into pre-synthesized vertically aligned MWNT arrays. The arrays were synthesized by ethylene chemical vapor deposition at 750 °C on silicon dioxide-silicon wafers using a water-assisted carbon etching as described elsewhere [10]. The free standing films have high porosity (95-99%) and are able to incorporate about 3 to 45 times TNA by mass (see Supplementary Fig. S1). A subsequent sodium azide (NaN_3)/water solution applied after wet impregnation allowed for facile initiation after drying for 24 hours at ambient temperature and pressure. Scanning electron microscopy (see Supplementary Fig. S3) shows that the alignment is preserved after wet impregnation. Transmission electron microscopy (Fig. 1b) indicates annular coatings of TNA crystals between 6 to 9 nm in thickness wrapping MWNTs of approximately 22 nm in diameter with an average of 10 walls. Alternate growth conditions (see Supplementary Fig. S2) produce 13-nm-diameter MWNTs with an average of nine walls, also explored in this work. The TNA coatings were uniform, although larger crystallites with defined grain boundaries were frequently visible along the side-walls of MWNTs, as shown in Fig. 1b, from homogeneous crystallization in the bulk impregnation solution before adsorption to the nanotubes. The x-ray diffraction (Fig. 1c, see Supplementary Fig. S4) spectra show that both the crystal structures of the bulk MWNT array and the TNA are preserved in the composite, with little evidence of organic intercalation [11-13]. The diffraction peak at 26° (002) corresponds to a typical inter-planar spacing of graphite (0.34 nm), and 42.4° (100) yields a 2.12 nm distance between neighboring nanotubes [14-16].

Two methods were used for initiating reactive waves in this system: laser irradiation and high voltage electrical discharge. The TNA-MWNT structures were either preheated or left at 300 K before ignition, and the reaction propagation and its velocity were measured by using a

microscope-aligned optical fiber array (see Supplementary Fig. S5) and high speed video microscopy (up to 90000 frames/sec) (see Supplementary Fig. S6), respectively, as shown in Fig. 2a. Sustained reaction waves specifically along the direction of the nanotube orientation (Fig. 2a, inset) were observed at velocities more than four orders of magnitude larger than the bulk combustion rate of TNA of 0.2 – 0.5 mm/s [17-20] at an atmospheric condition (1 atm). Several control materials confirm that the reaction wave requires the aligned nanotubes and TNA. Randomly oriented arrays, or those lacking TNA or NaN_3, showed no such sustained reaction in any direction under any condition. In the example in Fig. 2a, the aligned TNA-MWNT produced a steadily propagating wave with velocity 1.2 ± 0.4 m/s along the nanotube length. The MWNT generally survive the propagation of the wave intact, consistent with the high temperature stability of MWNT observed up to 3800 K[21,22]. To confirm that the mechanism of amplification involves the nanotube specifically as a thermal conduit, the reaction velocity dependence on preheating temperature (Fig. 2b) was measured both in parallel and orthogonal directions to the nanotube alignment. Both orientations demonstrated an increase in reaction velocity with increasing preheat temperature, but in the parallel orientation, where the external heat directly supplements that supplied by the reactive wave, the enhancement is nearly 10 times faster than the orthogonal orientation. The results from several velocity measurements are plotted in Fig. 2c for comparison. We found that 22-nm (10 walls) MWNT amplified the reaction velocity by more than 10000 times, while for 13-nm (9 walls) MWNT the enhancement was about 1000 times the TNA value. The difference is greater than what is predicted by the factor of 3 larger cross-sectional area of the 22-nm MWNT. A lower degree of alignment and higher quantity of amorphous carbon generated during synthesis of the 13-nm samples compared to the 22-nm samples accounts for apparent differences in conductances (see Supplementary Fig. S2).

Experimental geometries and a histogram of reaction front velocities for 92 devices appear in Supplementary Information (see Supplementary Fig. S7).

We adapt the theory of conventional combustion waves to describe the nanotube-coupled thermal wave. Consider a first order reactive annulus at dimensionless temperature *u* surrounding a nanotube or nanowire (Fig. 1a) at temperature u_2 where both are thermally coupled via a dimensionless interfacial conductance, γ. The Fourier description of this system is:

$$\frac{\partial u}{\partial \tau} = \frac{\partial^2 u}{\partial \xi^2} + (1-\eta)e^{-1/u} - \gamma_1 (u - u_2) \tag{1}$$

$$\frac{\partial u_2}{\partial \tau} = \alpha_0 \frac{\partial^2 u_2}{\partial \xi^2} + \gamma_2 (u - u_2) \tag{2}$$

$$\frac{\partial \eta}{\partial \tau} = \beta (1-\eta) e^{-1/u} \tag{3}$$

where η is the extent of chemical conversion of the reactive annulus, α_0 is the dimensionless thermal diffusivity of the nanotube (normalized by that of the annulus), β is the dimensionless inverse adiabatic temperature of the reactive annulus, τ and ξ are dimensionless time and distance. (Here, γ_1 and γ_2 are γ scaled by material properties of the annulus and nanotube, respectively.) A system initially at room temperature ($u_{atm} = u = 0.0124$ for TNA) will produce a reactive wave solution if one end is heated to ignition. Numerical solution of (1-3) demonstrates that, since the thermal conductance in the nanotube exceeds that of the reactive annulus, the reaction velocity along the nanotube component is increased substantially, directing the energy along its length. The interfacial conductance becomes insignificant beyond a minimum threshold ($\gamma_1 > 10^{-3}$, $\gamma_2 > 10^{-2}$ for $\beta > 5$) above which heat exchange between the phases is not rate-limiting (see Supplementary Fig. S12). In this case, the effect of thermal resistance between TNA and CNT

would be very small, and rapid thermal equilibrium is achieved on the boundary in the narrow reaction zone between the two materials ($T \approx T_2$). Under these conditions, higher interfacial conductance cannot change the temperature profile. The non-linear nature of the source term causes the reaction velocity to increase disproportionately with an increase in nanotube thermal diffusivity above that of the reactive annulus, creating an amplified thermal wave, as shown in Fig. 2c. The numerical solution of Fig.2c can be used in conjunction with the measured reaction velocities to estimate the effective thermal conductances of the MWNT. We find these values to be high, on average $2.1 \pm 0.32 \times 10^{-10}$ W/K for 22-nm-diameter MWNT. The value for 13-nm-diameter MWNT is $2.7 \pm 1.0 \times 10^{-11}$ W/K. For comparison, this is equivalent to a value of about 1,280 ± 200 W/m/K for an effective thermal conductivity of a 22-nm-diameter MWNT of height 2.36 mm (using the total MWNT cross section, including interior void space). The corresponding cross-sectional conductance, 4.5×10^5 W/m^2/K, is substantial, but only 0.01% of the theoretical upper bound of $10^9 - 10^{10}$ W/m^2/K over the range of 300 to 1000 K estimated by quantum constraints [23]. If the temperature dependence is included for thermal conductivities [24,25], heat capacities [19,26] and thermochemical properties [17,26-28], one can predict the reaction velocity explicitly. This refined model predicts 1.3 m/s for the wave velocity, in agreement with what is observed experimentally.

We find that this directional thermal wave evolves a corresponding thermopower wave in the same direction, creating a high specific power electrical pulse of constant polarity. The nanotubes were contacted to an oscilloscope with Cu wires and an Ag paste in the arrangement shown in Fig. 3a. Laser initiation at one end resulted in a voltage oscillation peak (see Supplementary Fig. S8) of the same duration as the corresponding reaction wave, allowing us to calculate reaction

propagation velocity for the whole sample volume (see Supplementary Fig. S9). The voltage was positive for waves emanating from the positive electrode, indicating a pulse of majority electronic carriers traveling toward the negative electrode (Fig. 3b). This thermopower wave is distinct from conventional, static thermopower in that we see single polarity pulses (positive or negative) over the reaction duration for high velocity waves. A moving thermal gradient across the conductor would produce regions of maximum, minimum and zero voltages based on the Seebeck effect, for example. This is in fact what we observe for samples with larger thermal mass and slower propagation velocities. Also, if the reaction is initiated at the middle of the sample, the current appears to reverse (Fig. 3c). In contrast, the chemically driven thermopower waves in the high velocity regime (Fig. 3b) have constant polarity always in the direction of the reaction. The results suggest that the wave traverses the system faster than the cooling time of the posterior region, resulting in a highly efficient energy direction. Carbon nanotubes have a relatively low Seebeck coefficient (80 μV/K) [29] compared with many thermoelectric materials, such as bismuth telluride (287 μV/K) [30] or Bi_2Te_3/Sb_2Te_3 superlattices (243 μV/K) [31], although modest increases are observed over the temperature range of 300 K and 930 K [32]. Thermopower waves, however, do not necessarily require low phonon and high electron transport rates as the thermal gradient is preserved in the propagation of the wave front. We note that materials with low figures of merit for thermoelectric devices can still produce high efficiencies for guiding thermopower waves, motivating a re-examination of these materials for thermal to electrical energy conversion.

Examining the specific power as a function of sample mass (Fig. 3d) for 115 devices demonstrates a significant sample-to-sample variation, mostly due to differences in reaction velocities. However, the maximum values observed exceed 7 kW/kg, and are substantially larger than those

for even high performance Li-ion batteries that have much slower discharge rates. Moreover, these high specific power values were observed as the sample mass decreased, a scaling trend that is very favorable for powering micro- and nano-scale devices. One explanation for this trend is that since all the samples had similar lengths (between 3 and 6 mm), a larger sample mass corresponds to a larger cross-sectional area and, therefore, increased orthogonal heat propagation that would eventually cause an overall system loss in an anisotropic reaction velocity (see Supplementary Fig. S9). To illustrate this further, high speed video microscopy was used in Fig. 4a to map the reaction front velocities as a function of orientation angle from the initiation point for an array of relatively large mass. Along the zero-degree axis (parallel to the nanotube orientation), the reaction propagates 6 to 13 times faster than in the orthogonal direction. As the number of parallel nanotubes in the array increase with mass, a greater fraction of heat travels orthogonal to the wave propagation, slowing its velocity and reducing the specific power (see Supplementary Fig. S9). The scaling trend is somewhat predicted by accounting for the change in reaction velocity with the system size and using a conventional thermopower model. In this case the specific power P/M_t is:

$$\frac{P}{M_t} = \frac{S^2}{R_i \rho \pi r^2 L} \int_0^L \frac{dT}{dL} dL \qquad (4)$$

where S is the Seebeck coefficient of nanotubes, R_i is electrical resistance, ρ is the density of the nanotubes, r is the radius of the nanotubes, L is the conduction length, and T is spatially defined temperature (Fig. 3d). A large mass sample generates a slower reaction velocity due to orthogonal heat dissipation. The temperature at the initial reaction position is related to the cooling time and the velocity of thermal wave. A relatively fast cooling time with a slow reaction

velocity causes a reverse temperature gradient and a diminution of specific power in the direction of wave propagation.

While predicting the general trend with system mass, we note that this model under-predicts the observed specific power by as much as 3000 W/kg in some cases. Hence, the nature of the induced thermopower current requires further study. There is an extensive literature on enhanced electron-phonon coupling in 1D-confined systems such as carbon nanotubes. This coupling manifests itself, for example, in the induction of electrical current with polar fluid flow over an array of CNTs [33], and negative differential conductance [34]. The thermopower waves, studied in this work for the first time, seem to propagate at only 0.0002% of a typical Fermi velocity. However, it is possible that the moving thermal gradient can entrain carriers such that a net drift velocity is measurable, and confine charge carriers in a narrow region of the reaction front. The nature of this supplemental power generation will be the subject of further research efforts.

In addition to the thermopower wave, the reaction creates a measurable pressure wave that is also of high energy density. The rapidly expanding, gaseous decomposition products from the thermal wave create a strong pressure pulse that is highly anisotropic. We measured the thrust force of this pressure wave using a micro-force sensor configuration (see Supplementary Fig. S13) to be substantially higher per total propulsion system mass than many other comparable micro-thrust generators in the literature [35-40]. The MWNT array was placed either normal or parallel to the force sensor surface, and immobilized in both directions during testing. Figure 4b illustrates the anisotropic nature of the thrust force. When perpendicular, the force peaks between 20 to 55

mN with a weak dependence on TNA loading, but in the parallel direction, the force was significantly reduced (< 9 mN). The relatively long duration reaction was obtained with TNA:MWNT mass ratio of 42 (max 47 mN, 175 ms duration) and 23 (max 35 mN, 200 ms duration). A reduction in loading ratio to 18 resulted in a larger peak thrust force (57 mN) for a shorter duration (110 ms). A smaller force is evolved (23 to 29 mN) as the ratio is further reduced to 5, but the reaction duration remains similar. The thrust reaches an optimal value at intermediate loading (loading ratio of 18) since increasing mass beyond this point increases the orthogonal heat transfer requirement. The broader line-shape of the reaction curves for loading ratios of 23 and 42 supports this. The magnitude of the evolved thrust per unit mass is extremely large in comparison to all other solid propellant microthrusters [35,40]. A free body experiment illustrates the directional nature of the evolved force (Fig. 4c). In this experiment, the system was released after initiation of the reaction, and its motion was recorded with a synchronized high speed camera. The instantaneous trajectory was compared with the orientation of the MWNT array at each frame, confirming the directional nature of the propulsion. It is an intrinsic property of this material that the thrust is evolved along a single axis, a property not yet realized in any other system. We compare the TNA-MWNT system to other published micro-thrusters with respect to the total and specific impulse per mass ratio (Fig. 4d) since these are the figures of merit for micro- or nano-scale actuator systems. Electrokinetic, ferromagnetic, laser ablation jet, and other systems [36,37,39] require bulky housings to direct and channel thrust, and thus have impulse per mass values many orders of magnitude less than the TNA-MWNT system. The total impulse per mass of TNA-MWNT (300 N-s/kg) is 4 to 100 times of that of other proposed micro-thrusters. The specific impulse per total mass (5.5 s/μg) is over 10 times that of typical solid propellant micro-thrusters [35,37,38,40].

The largest chemical to electrical and mechanical energy efficiencies observed in this work are 0.3 % and 0.12 % respectively, with the highest efficiency considering both as 0.42 %. The Carnot limit, set by the reaction temperature under adiabatic conditions, is a maximum of 80%. At the high decomposition temperatures explored in this work, the dominant parasitic heat loss is radiative. Engineering controls to prevent radiative losses may increase the efficiencies closer to this limit.

In summary, we have generated and measured anisotropic thermopower waves for the first time. These waves are produced by coupling an exothermic decomposition reaction of TNA to heat transfer in a MWNT conduit with high thermal conductivities calculated effectively to be 1.28 ± 0.2 kW/m/K in the range of 300 to 2860 K. The conduit accelerates the reaction along its length, creating a unidirectional thermal wave that is up to 10000 times faster than the bulk. This thermal wave also drives a thermopower wave, and we show that this results in high power densities up to 7 kW/kg, larger than Li-ion battery technology. This high specific power is seen in the limit of the smallest mass samples. The thermal wave is accompanied by a pressure wave of decomposing reaction products, resulting in exceedingly high total impulse per mass of 300 N-s/kg and specific impulse per total mass (5.5 s/μg). These systems represent a new class of single-use power sources for MEMS and NEMS applications, with very large power densities.

Figure legends

Figure 1 | Schematic of an exothermic chemical reaction guided along a thermally conducting CNT and experimental realization of MWNT encapsulated by cyclotrimethylene trinitramine (TNA). a, Ignition at one end of TNA-CNT results in an exothermic reaction and heat transfer along the length of the CNT, with feedback creating an anisotropic reaction wave of amplified velocity. **b,** Transmission electron microscopy image of TNA-MWNT synthesized by wet impregnation. The dashed line indicates the boundary between MWNT and TNA layers. **c,** X-ray diffraction showing TNA-MWNT after synthesis (black), MWNT only (blue) and TNA only (red).

Figure 2 | An accelerated, anisotropic reaction wave of TNA confined to an annular region around a nanotube thermal waveguide. a, Reaction propagation along an aligned MWNT array (average diameter 22 nm) after ignition by electrical discharge (no preheating). The height of the TNA-MWNT array is ~2 mm, and its cross-section is about 0.1 mm^2 (frame rate = 3.33 kHz). **b,** The reaction velocity differs between samples preheated parallel and orthogonal to the aligned direction (average MWNT diameter 13 nm) as measured with an optical fiber array along the array length (see Supplementary Fig. S5). The x-axis shows the preheating temperature of the TNA-MWNT array (Table S1). **c,** Predicted reaction velocity from the Fourier model (equations 1-3) as a function of β, the dimensionless inverse adiabatic temperature of the annular material (10.6 for TNA, Table S2) versus CNT thermal diffusivity (m^2/s). Note that the reaction velocity increases with increasing CNT thermal conductance. Experimentally observed reaction velocities for both 13- and 22-nm MWNT are plotted for comparison.

Figure 3 | A chemically driven thermopower wave. a, Illustration of the experimental setup used for measuring the corresponding thermopower waves that result from reaction wave propagation. Laser ignition (or electric arc discharge) at one end results in a thermopower wave in the same direction of reaction propagation; either positive or negative voltage generation is observed. **b,** The DC voltage generated by exothermic reaction of TNA is observed immediately after laser ignition with a single polarity peak voltage in this experiment of 30 – 35 mV (max observed = 210 mV) in both positive and negative directions for a total system mass of 0.8 mg with a TNA/MWNT ratio of 9. **c,** These thermopower waves appear distinct from conventional, static thermopower generation mechanisms. If the system mass is increased, the reaction wave moves slowly and multiple peaks are observed instead, showing a reversal of polarity and an inflection point. Similar behavior is seen if initiation occurs at the center of the sample. **d,** The specific peak power plotted as a function of system mass for three different TNA/MWNT mass ratios (9, 4.5, and 2.8) and two different MWNT with diameters (13 and 22 nm) shows an inverse scaling, highlighting that the thermopower wave is enhanced at the micro-nanoscale, and can produce power densities that far exceed conventional energy storage devices. The green line is equation 4 based on the conventional thermoelectric effect and the temperature gradient from reaction (300 K-2800 K).

Figure 4 | Anisotropic reaction propagation. a, For larger samples, there remains a large axial component to the reaction wave, but also a portion that is orthogonal. The reaction velocities

along the aligned (0^o) and orthogonal (90^o) directions show a discernable peak along the axial direction. (Reactions were initiated at the base.) Parenthetical numbers are the mass ratio and mass of TNA. **b,** The thermopower wave evolves a thrust force of commensurate duration. The transient force response is larger for the 5 samples (5 x 5 x 6 mm, 5–20 mg) aligned perpendicular to the sensor compared with the control aligned parallel to the surface. **c,** An illustration of directed thrust: moving as a free body, the TNA-MWNT array (0.4 x 0.3 x 2 mm) proceeds in the direction of its orientation without external confinement. **d,** The total impulse and specific impulse per total mass of TNA-MWNT is significantly higher than other micro-thruster systems [35-40] because of the lack of a need for external containment, in contrast to electrokinetic [37], ferroelectric plasma [39], and laser ablation jet [36] micro-thruster approaches.

References

1. Please, C. P., Liu, F. & McElwain, D. L. S. Condensed phase combustion travelling waves with sequential exothermic or endothermic reactions. *Combust. Theor. Model.* **7**, 129-143 (2003).
2. Zel'dovich, Y. B. & Frank-Kamenetskii, D. A. The theory of thermal flame propagation. *Zh. Fiz. Khim.* **12**, 100-105 (1938).
3. Roy, G. D., Frolov, S. M., Borisov, A. A. & Netzer, D. W. Pulse detonation propulsion: challenges, current status, and future perspective. *Prog. Energ. Combust.* **30**, 545-672 (2004).
4. Arimondi, M., Anselmi-Tamburini, U., Gobetti, A., Munir, Z. A. & Spinolo, G. Chemical mechanism of the Zr+O-2->ZrO2 combustion synthesis reaction. *J. Phys. Chem. B* **101**, 8059-8068 (1997).
5. Alexander, M. H. et al. Nitramine Propellant Ignition and Combustion Research. *Prog. Energ. Combust.* **17**, 263-296 (1991).
6. Yu, C. H., Shi, L., Yao, Z., Li, D. Y. & Majumdar, A. Thermal conductance and thermopower of an individual single-wall carbon nanotube. *Nano Lett.* **5**, 1842-1846 (2005).
7. Chang, C. W., Okawa, D., Garcia, H., Majumdar, A. & Zettl, A. Nanotube phonon waveguide. *Phys. Rev. Lett.* **99**, 045901-045904 (2007).
8. Chang, C. W., Okawa, D., Majumdar, A. & Zettl, A. Solid-state thermal rectifier. *Science* **314**, 1121-1124 (2006).
9. Akkutlu, I. Y. & Yortsos, Y. C. The dynamics of in-situ combustion fronts in porous media. *Combust. Flame* **134**, 229-247 (2003).
10. Hata, K. et al. Water-assisted highly efficient synthesis of impurity-free single-waited carbon nanotubes. *Science* **306**, 1362-1364 (2004).
11. Prevo, B. G. & Velev, O. D. Controlled, rapid deposition of structured coatings from micro- and nanoparticle suspensions. *Langmuir* **20**, 2099-2107 (2004).
12. Kulkarni, A. M. & Zukoski, C. F. Nanoparticle crystal nucleation: Influence of solution conditions. *Langmuir* **18**, 3090-3099 (2002).
13. Simchi, A., Ahmadi, R., Reihani, S. M. S. & Mahdavi, A. Kinetics and mechanisms of nanoparticle formation and growth in vapor phase condensation process. *Mater. Design* **28**, 850-856 (2007).
14. Yusa, H. & Watanuki, T. X-ray diffraction of multiwalled carbon nanotube under high pressure: Structural durability on static compression. *Carbon* **43**, 519-523 (2005).
15. Maniwa, Y. et al. Anomaly of X-ray diffraction profile in single-walled carbon nanotubes. *Jpn. J. Appl. Phys., Part 2* **38**, L668-L670 (1999).
16. Cao, A. Y., Xu, C. L., Liang, J., Wu, D. H. & Wei, B. Q. X-ray diffraction characterization on the alignment degree of carbon nanotubes. *Chem. Phys. Lett.* **344**, 13-17 (2001).
17. Volkov, E. N., Paletsky, A. A. & Korobeinichev, O. P. RDX flame structure at atmospheric pressure. *Combust. Explo. Shock.* **44**, 43-54 (2008).
18. Aleksandrov, V. V., Tukhtaev, R. K., Boldyrev, V. V. & Boldyreva, A. V. Mechanism of Catalytic Additive Effects on Diethylnitramine Dinitrate Combustion Rates. *Combust. Flame* **35**, 1-15 (1979).
19. Homan, B. E., Miller, M. S. & Vanderhoff, J. A. Absorption diagnostics and modeling investigations of RDX flame structure. *Combust. Flame* **120**, 301-317 (2000).

20. Zenin, A. Hmx and Rdx - Combustion Mechanism and Influence on Modern Double-Base Propellant Combustion. *J. Propul. Power* **11**, 752-758 (1995).
21. Miyamoto, Y., Berber, S., Yoon, M., Rubio, A. & Tomanek, D. Onset of nanotube decay under extreme thermal and electronic excitations. *Physica B* **323**, 78-85 (2002).
22. Begtrup, G. E. et al. Probing nanoscale solids at thermal extremes. *Physical Review Letters* **99**, 155901-155904 (2007).
23. Mingo, N. & Broido, D. A. Carbon nanotube ballistic thermal conductance and its limits. *Physical Review Letters* **95**, 096105-096108 (2005).
24. Hanson-Parr, D. M. & Parr, T. P. Thermal properties measurements of solid rocket propellant oxidizers and binder materials as a function of temperature. *J. Energetic Mat.* **17**, 1-47 (1999).
25. Li, S. C., Williams, F. A. & Margolis, S. B. Effects of 2-phase flow in a model for nitramine deflagration. *Combust. Flame* **80**, 329-349 (1990).
26. Liau, Y. C., Kim, E. S. & Yang, V. A comprehensive analysis of laser-induced ignition of RDX monopropellant. *Combust. Flame* **126**, 1680-1698 (2001).
27. Oyumi, Y. Melt phase decomposition of RDX and two nitrosamine derivatives. *Propell. Explos. Pyrot.* **13**, 42-47 (1988).
28. Long, G. T., Vyazovkin, S., Brems, B. A. & Wight, C. A. Competitive vaporization and decomposition of liquid RDX. *Journal of Physical Chemistry B* **104**, 2570-2574 (2000).
29. Kim, P., Shi, L., Majumdar, A. & McEuen, P. L. Thermal transport measurements of individual multiwalled nanotubes. *Phys. Rev. Lett.* **8721**, 215502-215505 (2001).
30. Takashiri, M., Takiishi, M., Tanaka, S., Miyazaki, K. & Tsukamoto, H. Thermoelectric properties of n-type nanocrystalline bismuth-telluride-based thin films deposited by flash evaporation. *J. Appl. Phys.* **101**, 074301-074305 (2007).
31. Venkatasubramanian, R., Siivola, E., Colpitts, T. & O'Quinn, B. Thin-film thermoelectric devices with high room-temperature figures of merit. **413**, 597-602 (2001).
32. Zhang, H. L. et al. Electrical and thermal properties of carbon nanotube bulk materials: Experimental studies for the 328-958 K temperature range. *Phys. Rev. B* **75**, 205407-205415 (2007).
33. Ghosh, S., Sood, A. K. & Kumar, N. Carbon nanotube flow sensors. *Science* **299**, 1042-1044 (2003).
34. Pop, E. et al. Negative differential conductance and hot phonons in suspended nanotube molecular wires. *Physical Review Letters* **95**, 155505-155508 (2005).
35. Zhang, K. L., Chou, S. K., Ang, S. S. & Tang, X. S. A MEMS-based solid propellant microthruster with Au/Ti igniter. *Sensors and Actuators A-Physical* **122**, 113-123 (2005).
36. Phipps, C., Luke, J., Lippert, T., Hauer, M. & Wokaun, A. Micropropulsion using a laser ablation jet. *J. Propul. Power* **20**, 1000-1011 (2004).
37. Patel, K. D. et al. Electrokinetic pumping of liquid propellants for small satellite microthruster applications. *Sens. Actuators, B* **132**, 461-470 (2008).
38. Kuan, C. K., Chen, G. B. & Chao, Y. C. Development and ground tests of a 100-millinewton hydrogen peroxide monopropellant microthruster. *J. Propul. Power* **23**, 1313-1320 (2007).
39. Kemp, M. A. & Kovaleski, S. D. Ferroelectric plasma thruster for microspacecraft propulsion. *J. Appl. Phys.* **100**, 113306-113311 (2006).
40. Chaalane, A., Rossi, C. & Esteve, D. The formulation and testing of new solid propellant mixture (DB plus x%BP) for a new MEMS-based microthruster. *Sens. Actuators, A* **138**, 161-166 (2007).

Acknowledgements

This work was supported primarily by a grant to M. S. S. from the Air Force Office of Scientific Research and from an NSF Career Award also to M. S. S. S. B. appreciates support by WCU (World Class University) program through the Korea Science and Engineering Foundation funded by the Ministry of Education, Science and Technology, Korea (R31-2008-000-10029-0). J. T. A. and W. J. C. acknowledge fellowship support from the National Science Foundation and ILJU, respectively. J. -H. H. acknowledges support from the Korea Research Foundation (MOEHRD, KRF-2006-214-D00117). We acknowledge T.M. Swager for help with TNA extraction.

Author contributions

W. J. C., M. S. S., and J.-H. H developed the concept. W. J. C. and S. H. carried out experiments. W. J. C. and J. T. A. conducted modeling and simulations. All authors contributed to data analysis and scientific discussion.

a

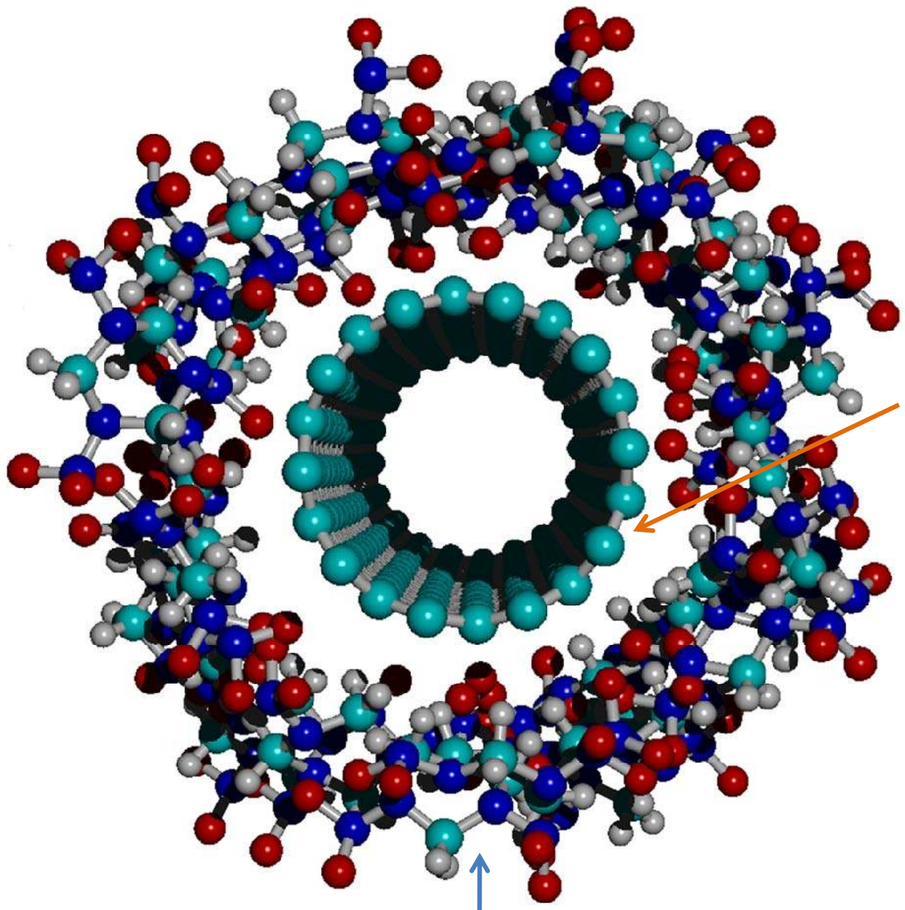
CNT
TNA layer around carbon nanotube (CNT)

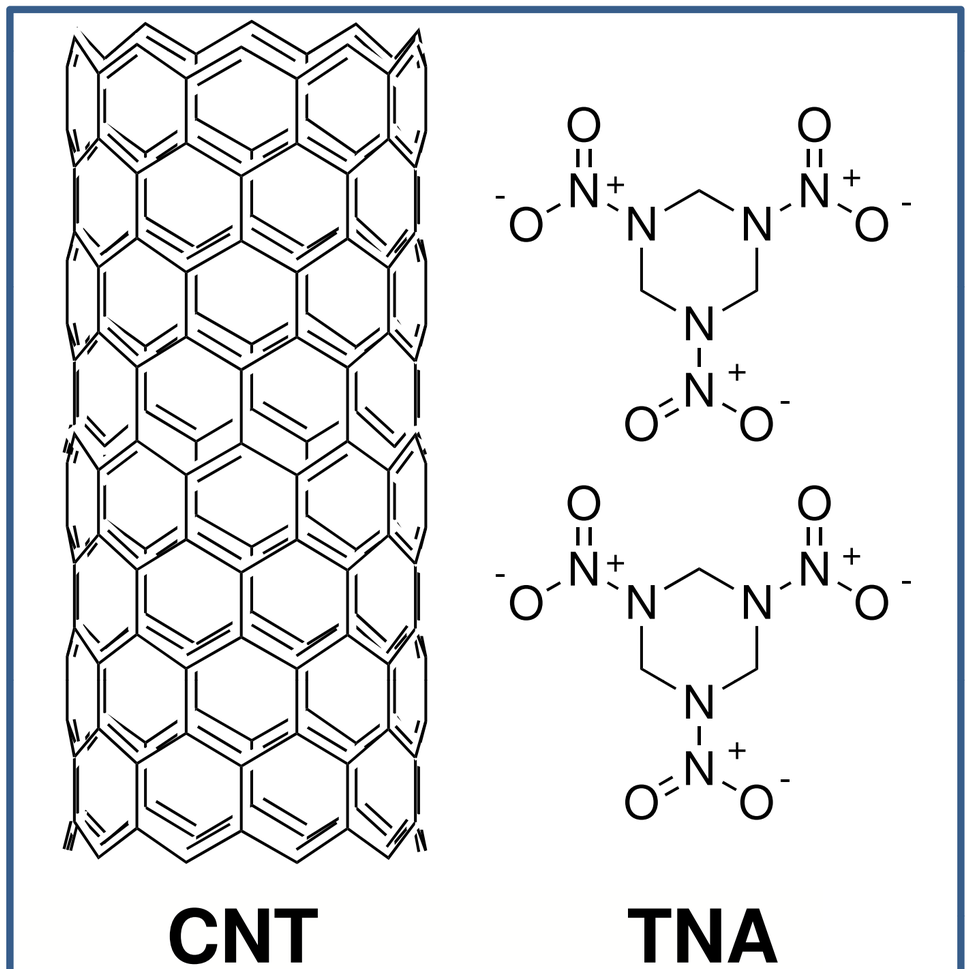
CNT
TNA

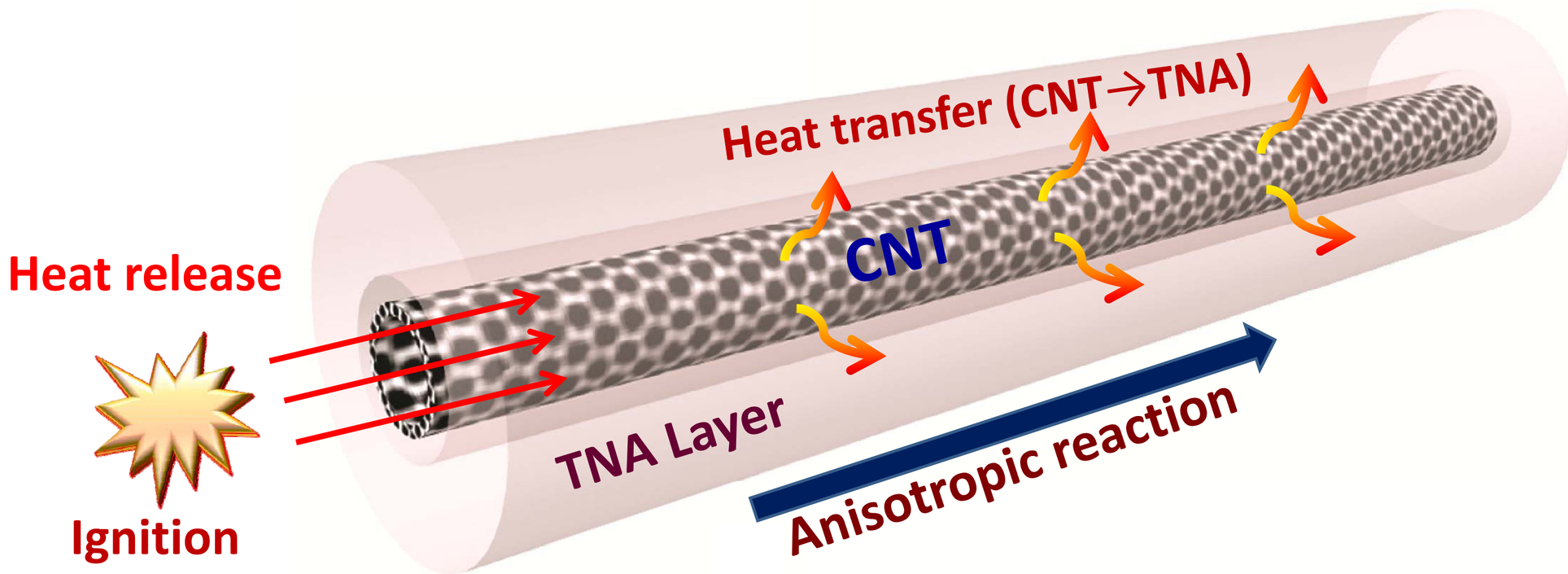
Heat release
Ignition
Heat transfer (CNT→TNA)
CNT
TNA Layer
Anisotropic reaction

b

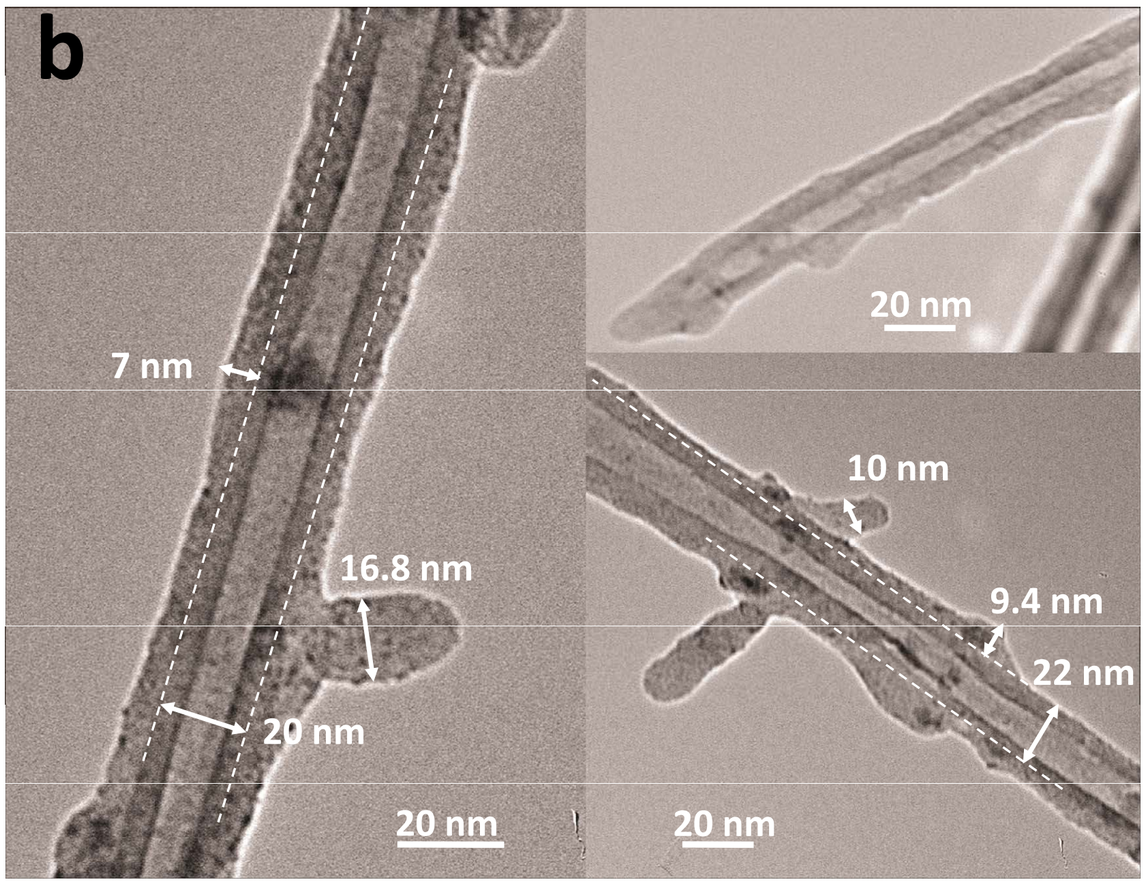
7 nm
16.8 nm
20 nm
20 nm
20 nm
10 nm
9.4 nm
22 nm
20 nm

c

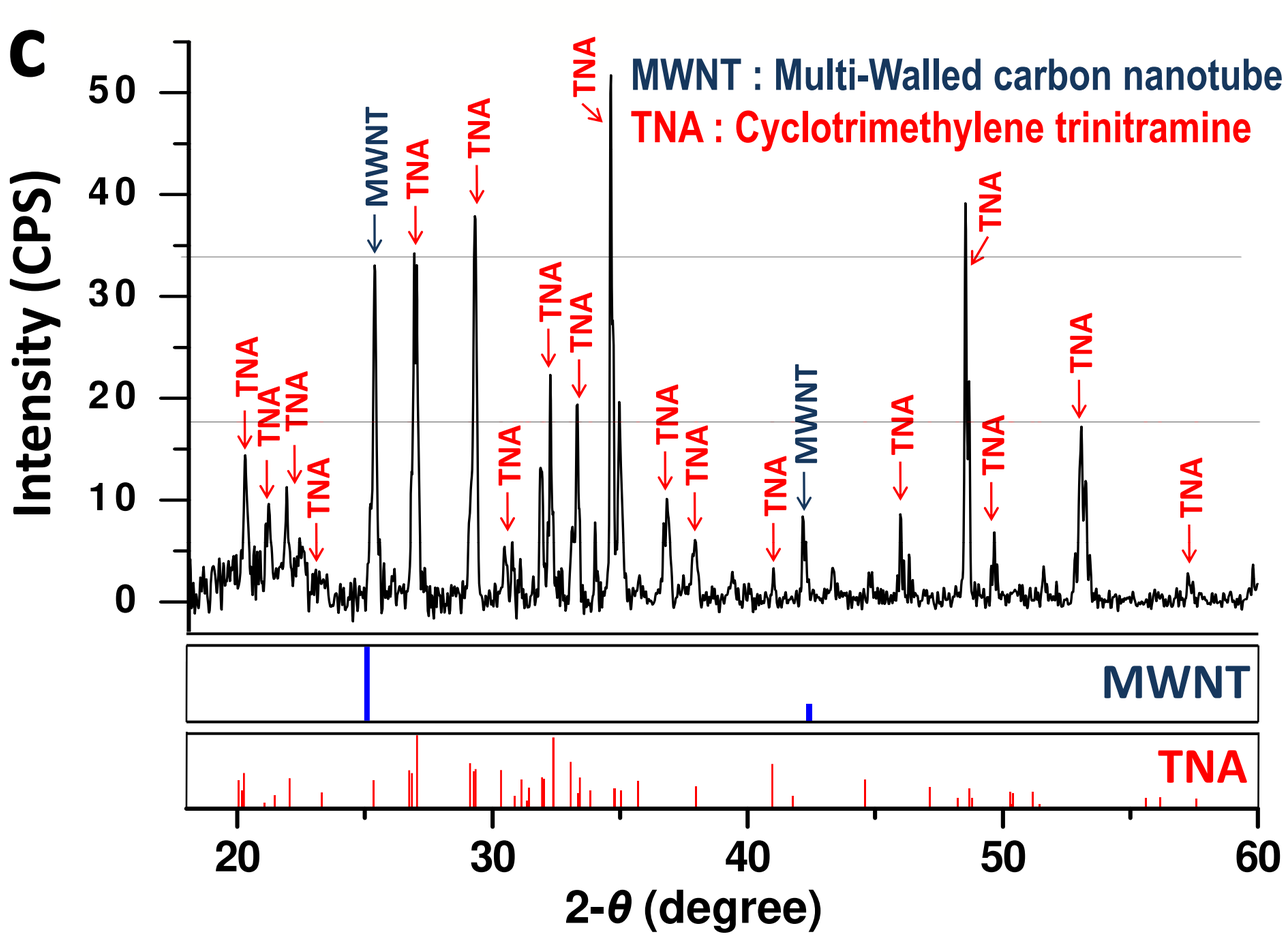
MWNT : Multi-Walled carbon nanotube
TNA : Cyclotrimethylene trinitramine
Intensity (CPS)
2-θ (degree)
MWNT
TNA

a

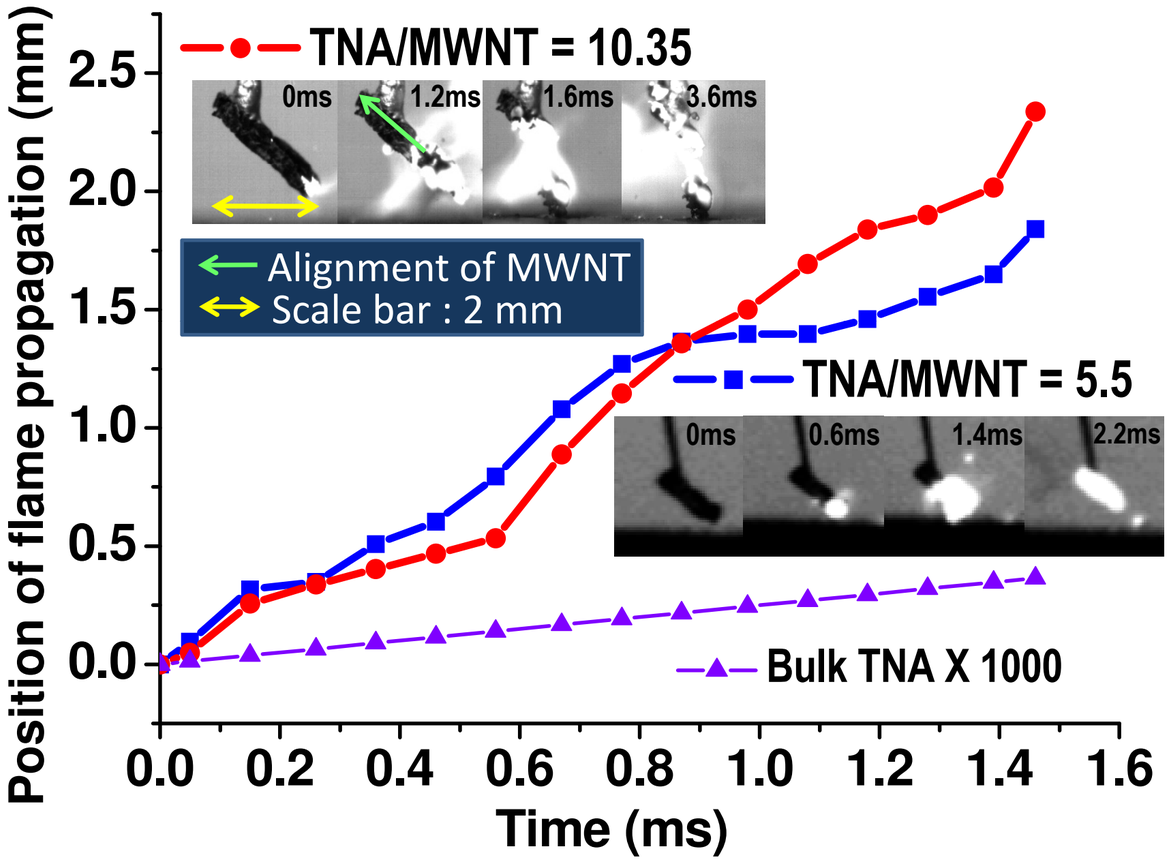
TNA/MWNT = 10.35
0ms
1.2ms
1.6ms
3.6ms
Alignment of MWNT
Scale bar : 2 mm
TNA/MWNT = 5.5
0ms
0.6ms
1.4ms
2.2ms
Bulk TNA X 1000
Position of flame propagation (mm)
Time (ms)

b

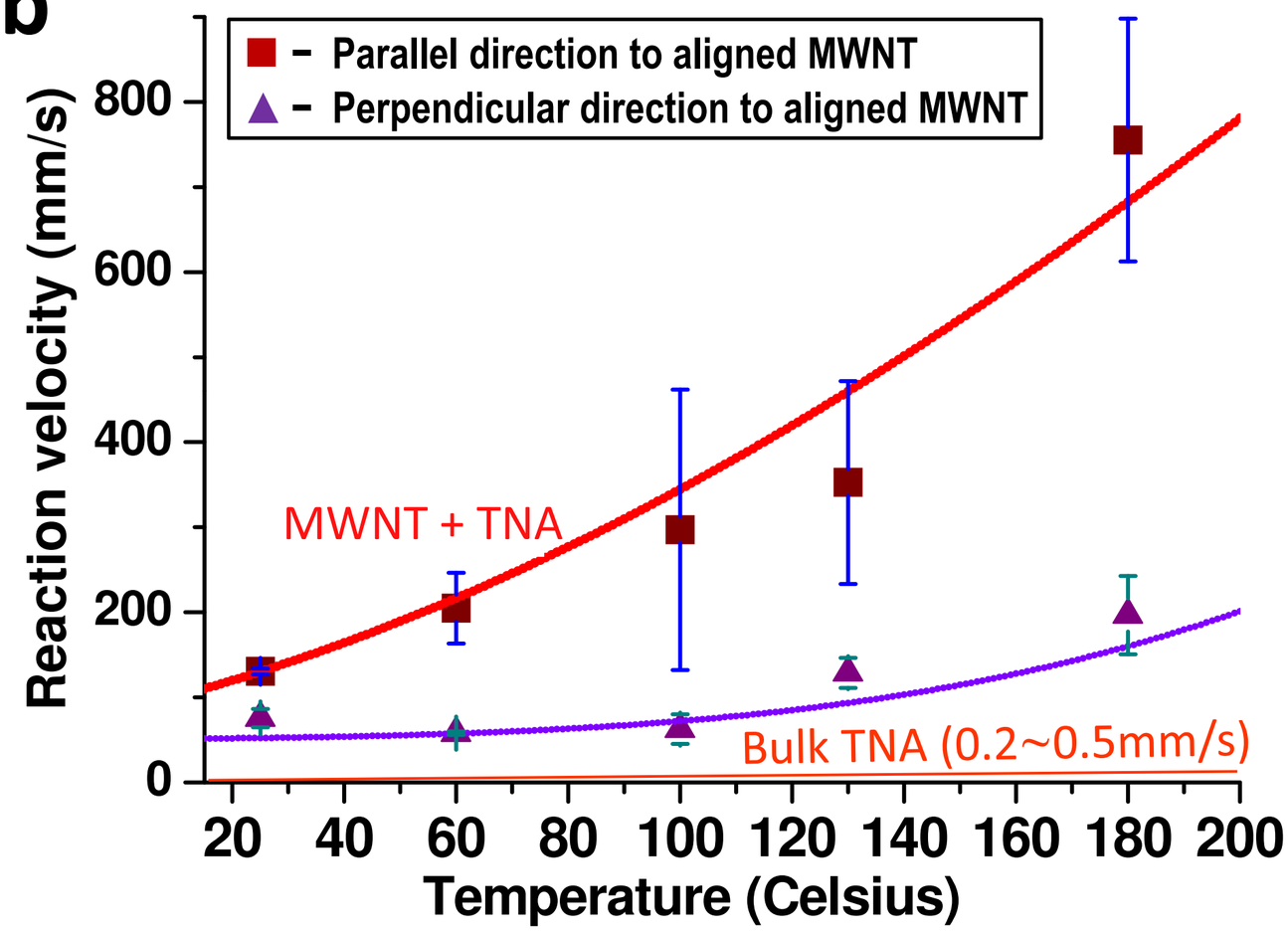
Parallel direction to aligned MWNT
Perpendicular direction to aligned MWNT
MWNT + TNA
Bulk TNA (0.2~0.5mm/s)
Reaction velocity (mm/s)
Temperature (Celsius)

c

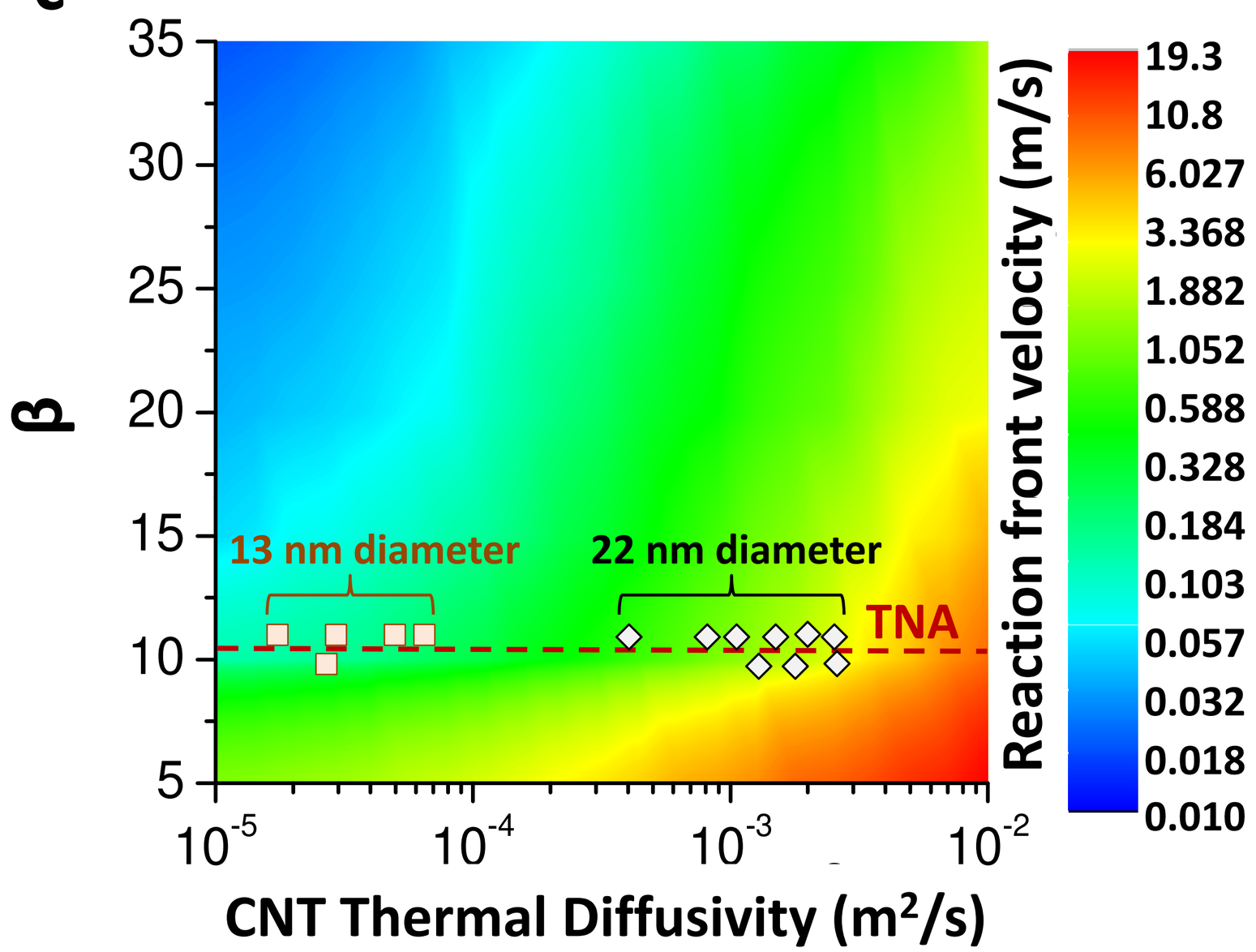
β
13 nm diameter
22 nm diameter
TNA
Reaction front velocity (m/s)
19.3
10.8
6.027
3.368
1.882
1.052
0.588
0.328
0.184
0.103
0.057
0.032
0.018
0.010
CNT Thermal Diffusivity (m²/s)

a

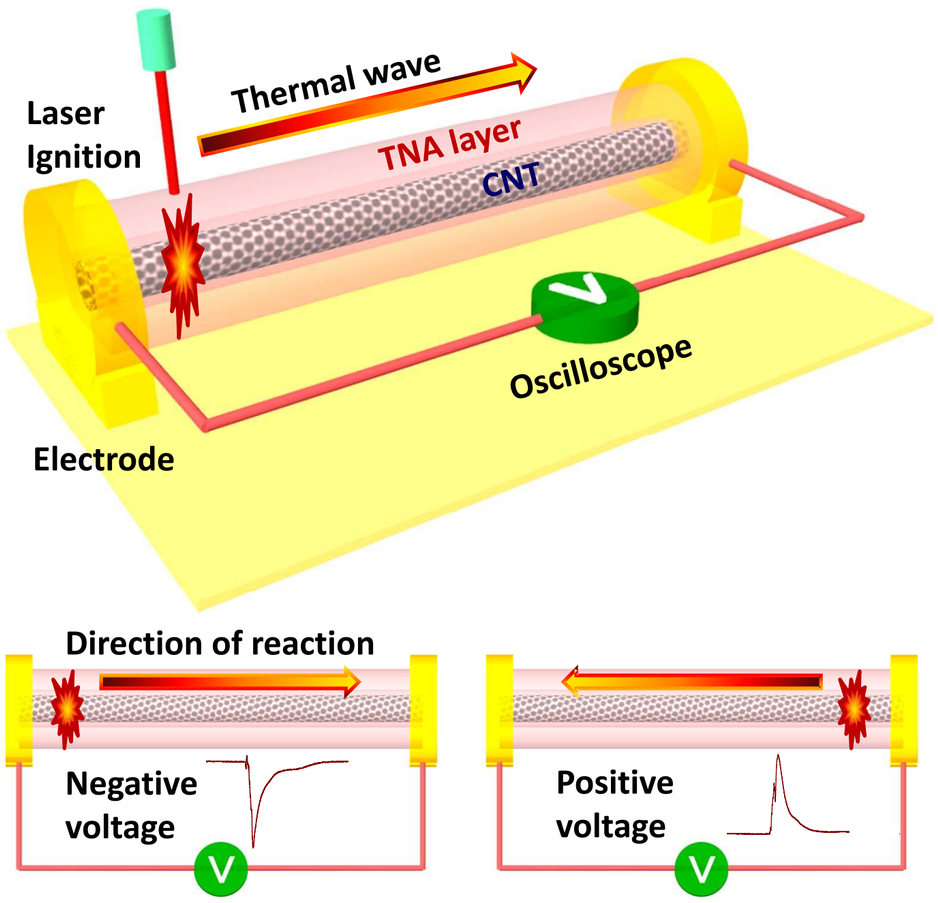
Laser
Ignition
Thermal wave
TNA layer
CNT
Oscilloscope
Electrode
Direction of reaction
Negative
voltage
Positive
voltage
V

b

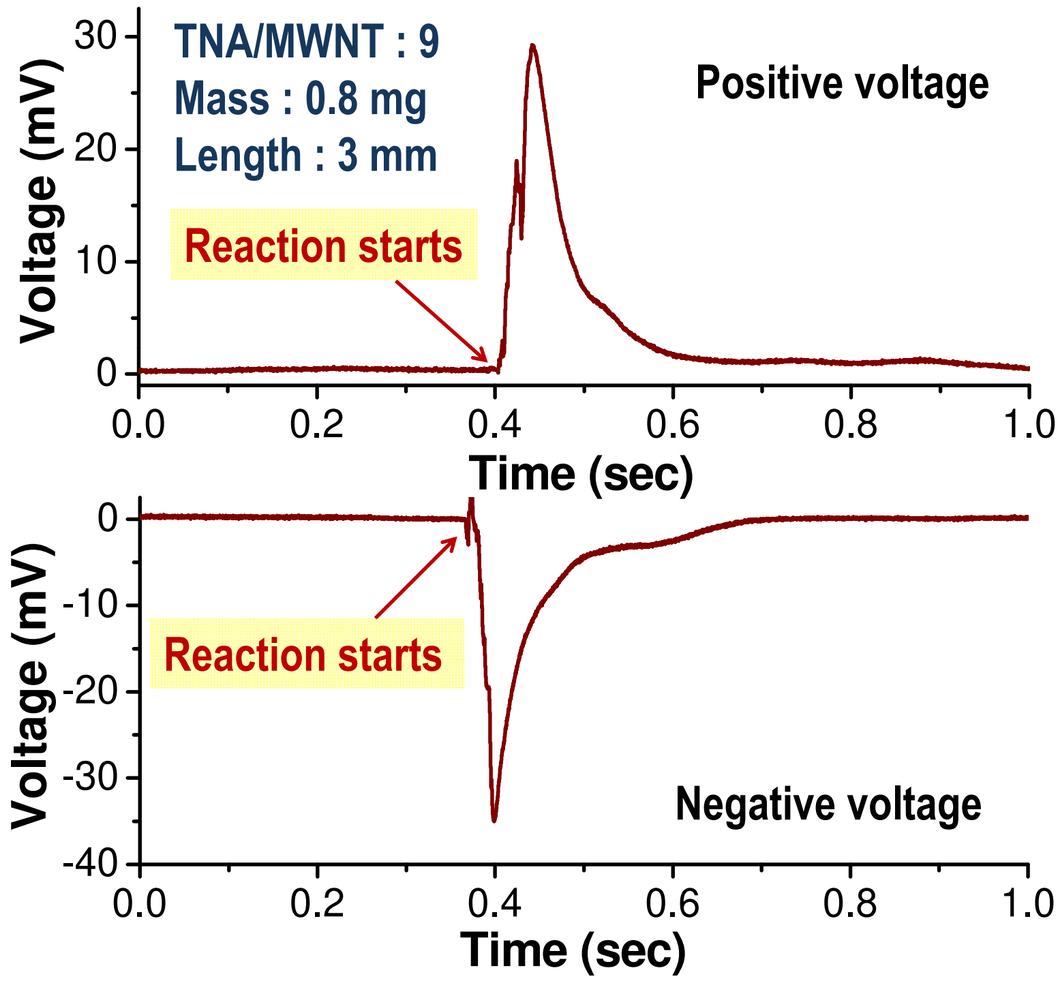
TNA/MWNT : 9
Mass : 0.8 mg
Length : 3 mm
Reaction starts
Positive voltage
Voltage (mV)
Time (sec)
Reaction starts
Negative voltage
Voltage (mV)
Time (sec)

c

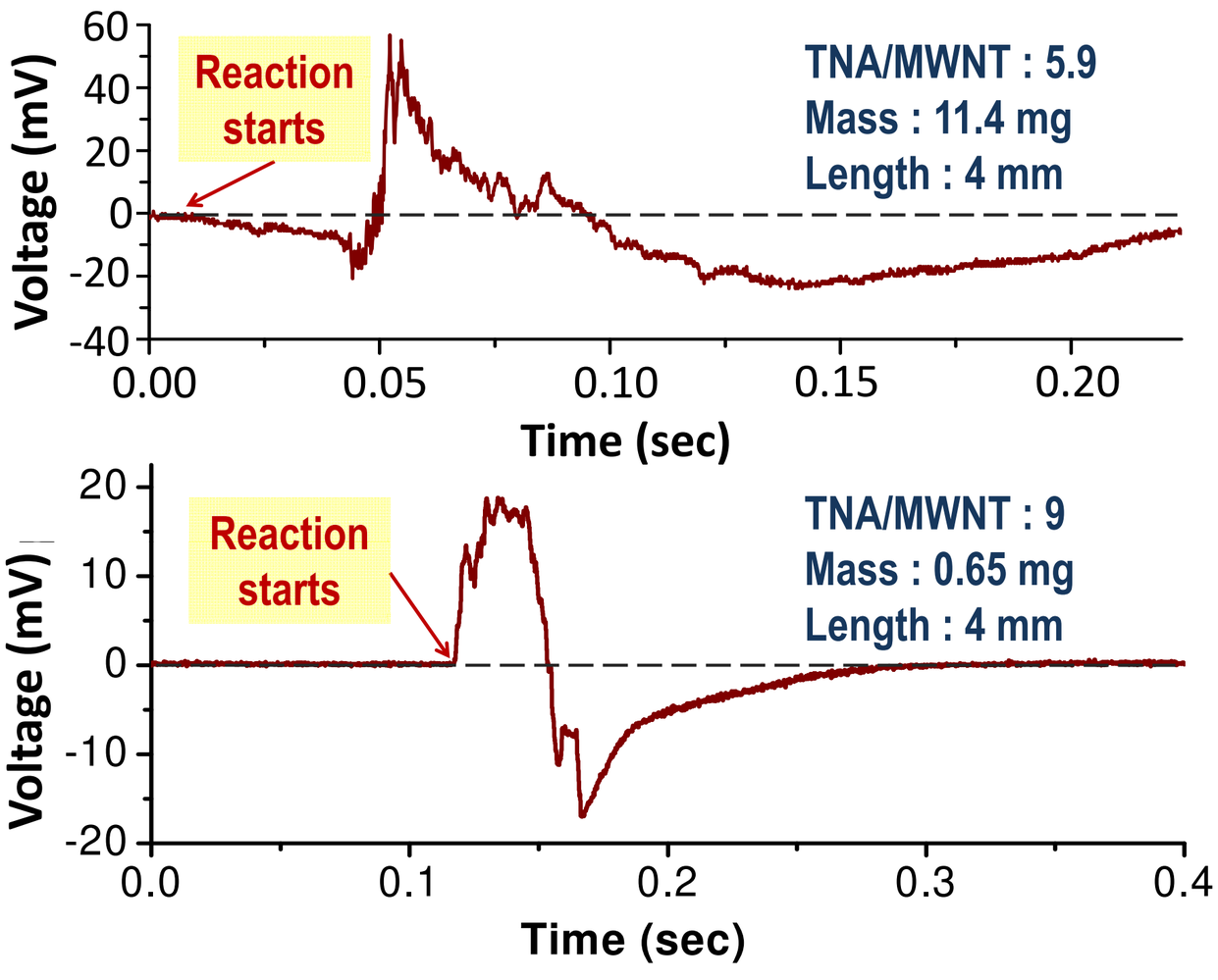
Reaction
starts
TNA/MWNT : 5.9
Mass : 11.4 mg
Length : 4 mm
Voltage (mV)
Time (sec)
Reaction
starts
TNA/MWNT : 9
Mass : 0.65 mg
Length : 4 mm
Voltage (mV)
Time (sec)

d

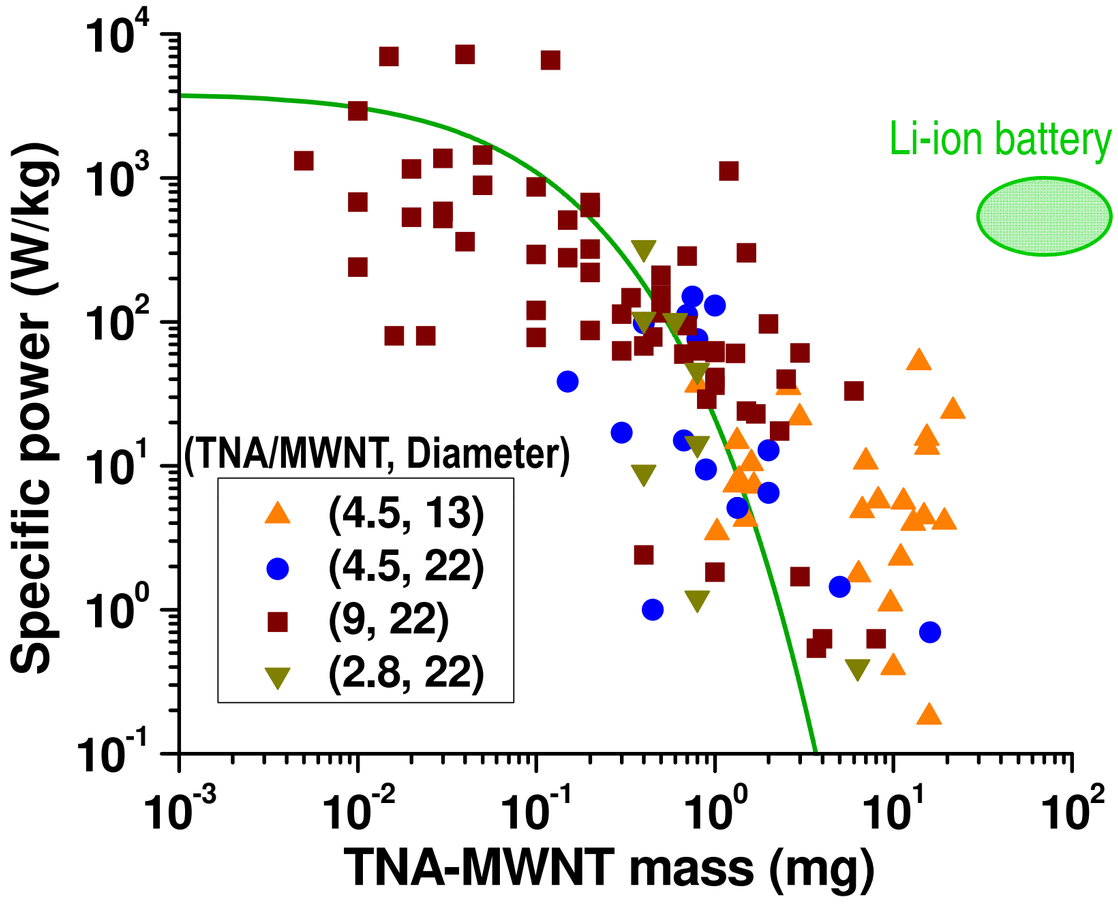
Li-ion battery
(TNA/MWNT, Diameter)
(4.5, 13)
(4.5, 22)
(9, 22)
(2.8, 22)
Specific power (W/kg)
TNA-MWNT mass (mg)

a

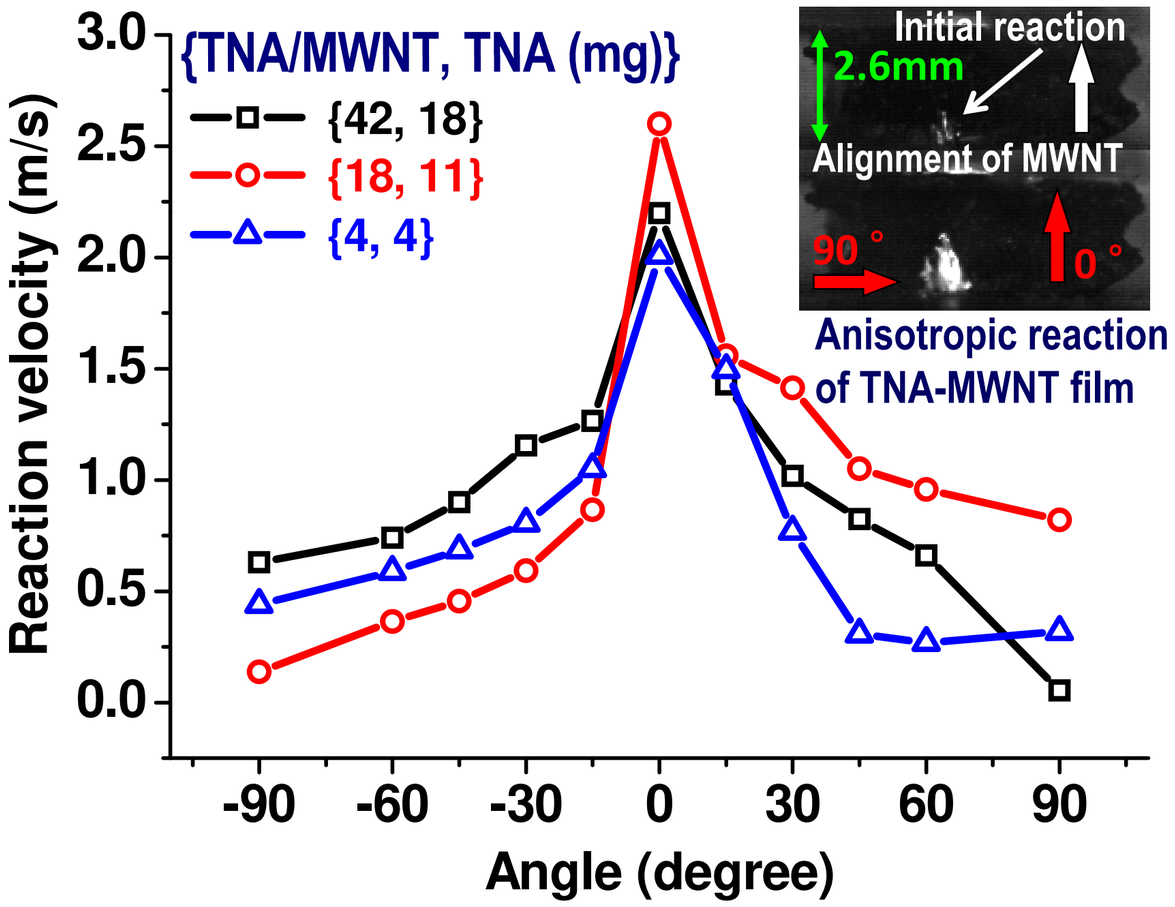
{TNA/MWNT, TNA (mg)}
{42, 18}
{18, 11}
{4, 4}
Reaction velocity (m/s)
Angle (degree)
Initial reaction
2.6mm
Alignment of MWNT
90 °
0 °
Anisotropic reaction
of TNA-MWNT film

b

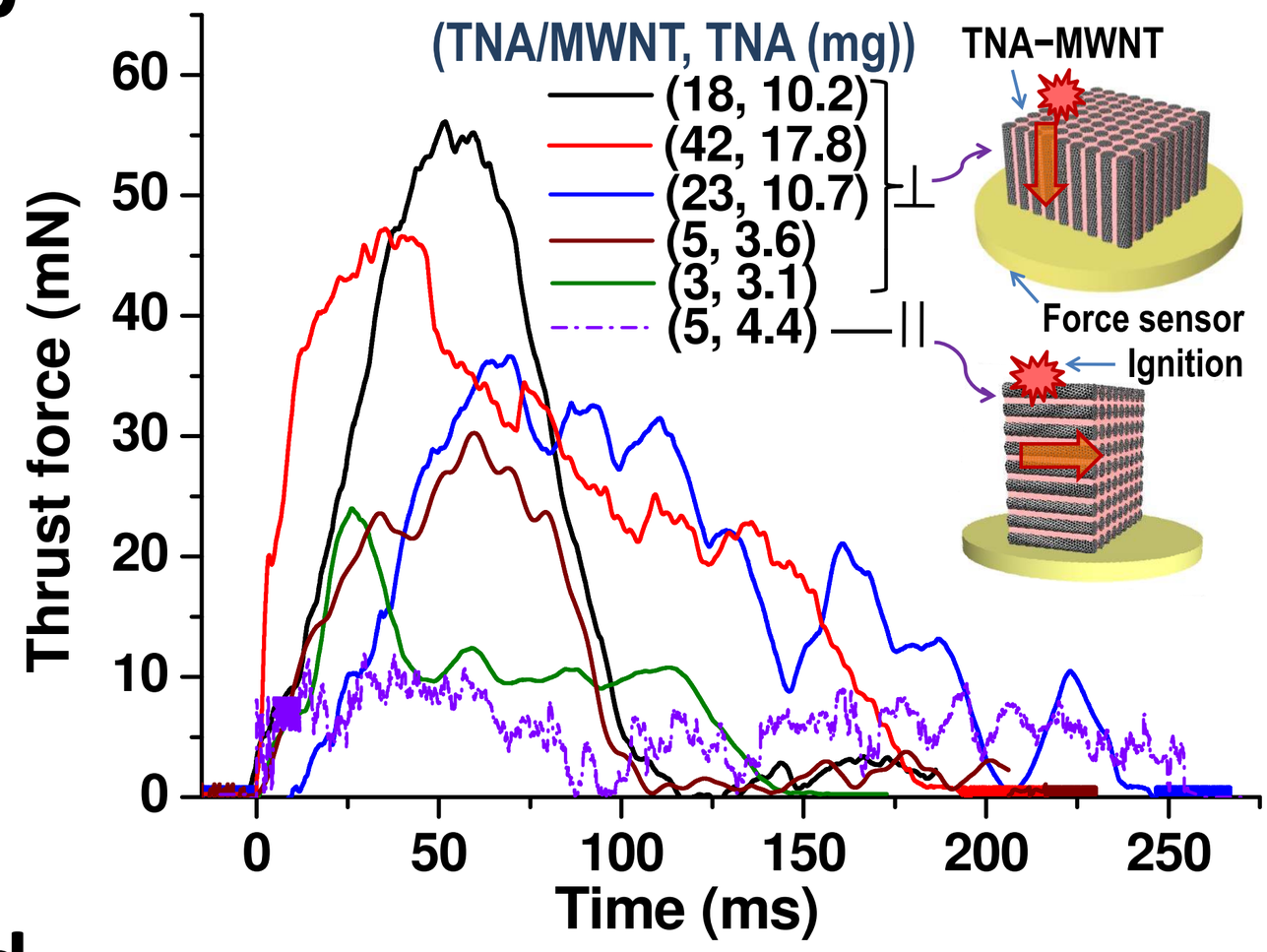
(TNA/MWNT, TNA (mg))
(18, 10.2)
(42, 17.8)
(23, 10.7)
(5, 3.6)
(3, 3.1)
(5, 4.4)
TNA–MWNT
Force sensor
Ignition
Thrust force (mN)
Time (ms)

c

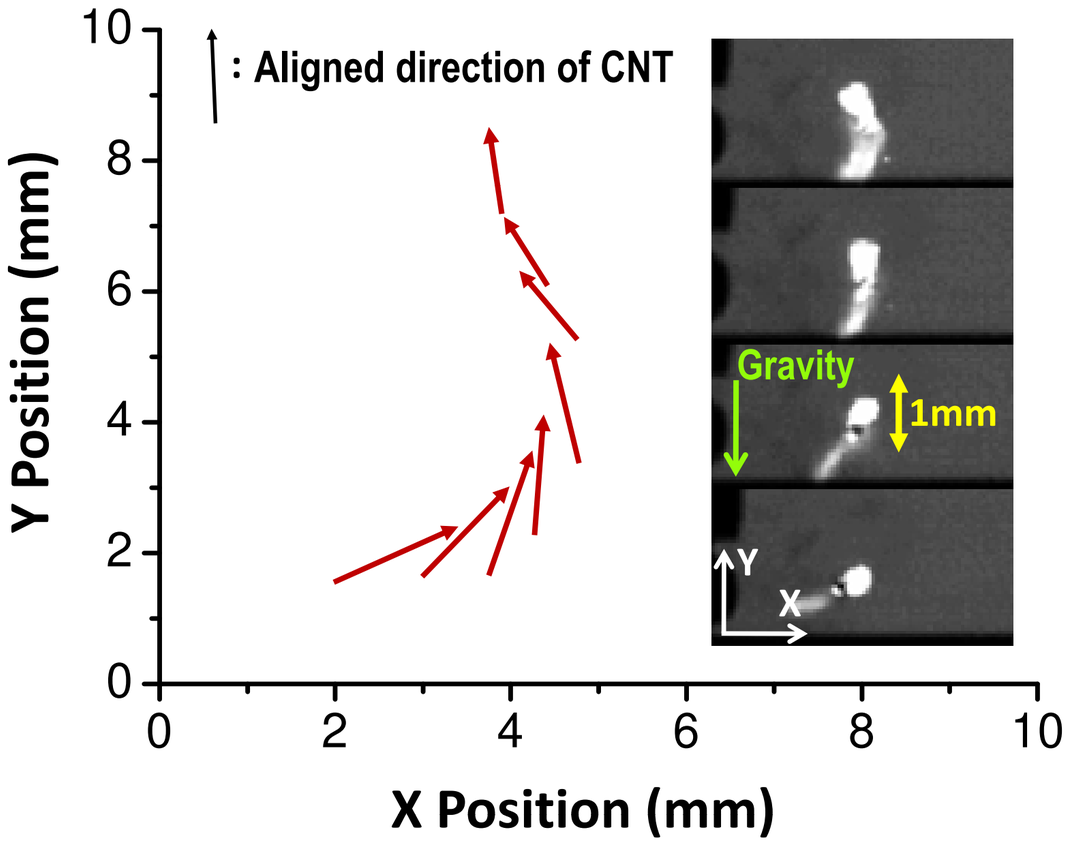
: Aligned direction of CNT
Gravity
1mm
Y
X
Y Position (mm)
X Position (mm)

d

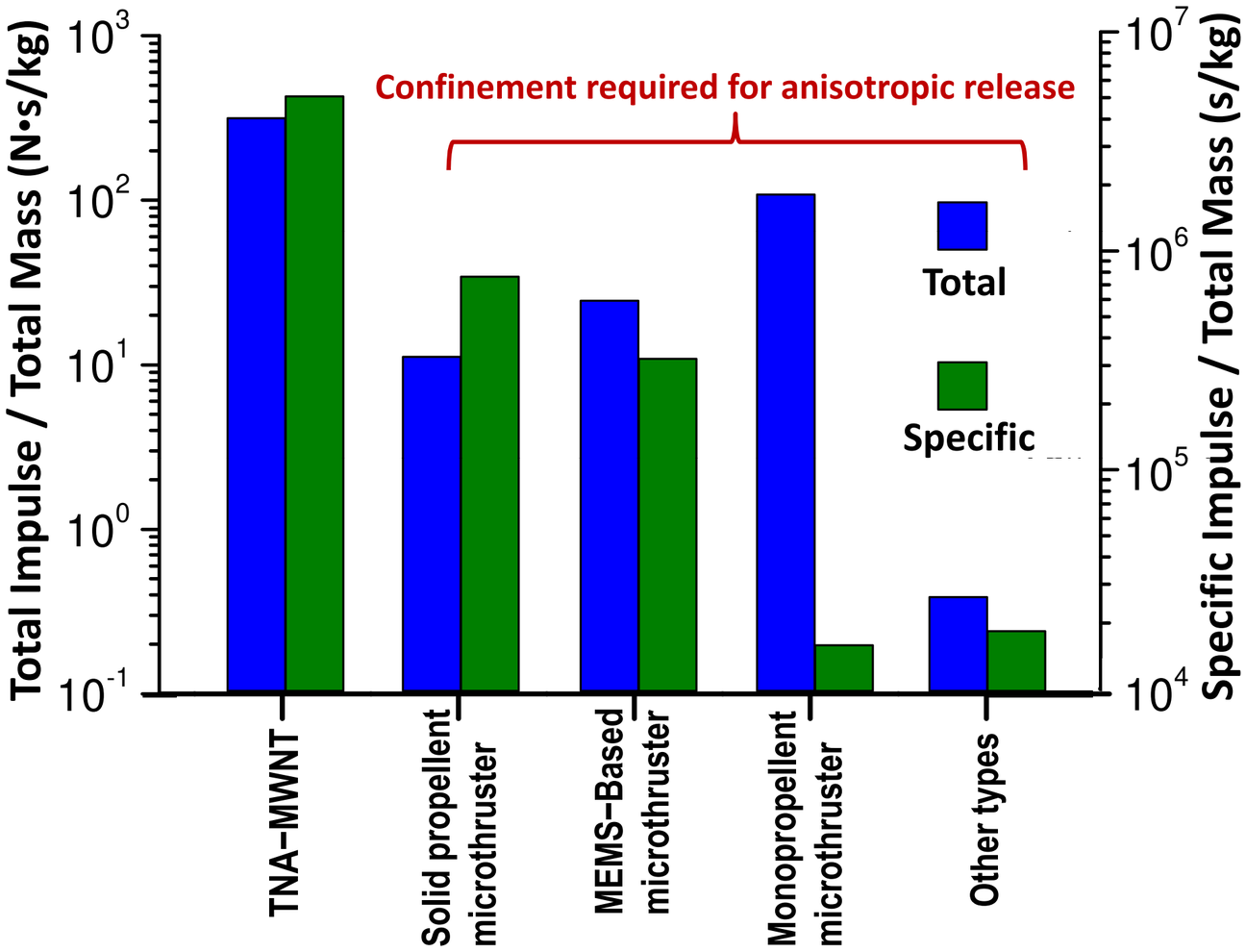
Confinement required for anisotropic release
Total
Specific
Total Impulse / Total Mass (N•s/kg)
Specific Impulse / Total Mass (s/kg)
TNA–MWNT
Solid propellent microthruster
MEMS–Based microthruster
Monopropellent microthruster
Other types

SUPPLEMENTARY INFORMATION

Materials and methods

1. Synthesis of Vertically Aligned Multi-walled Carbon Nanotubes

Vertically aligned multi-walled carbon nanotubes (VAMWNT) were synthesized by the chemical vapor deposition (CVD) method in a horizontal quartz tube furnace with an inner diameter of 29 mm. Catalyst layers, 0.5 – 1 nm Fe and 10 nm Al_2O_3, were deposited on a silicon wafer by electron beam evaporation [1]. Ethylene (C_2H_4) was the carbon source. Hydrogen (H_2) and argon (Ar) were used as catalytic and carrier gases, respectively [2]. The gases were preheated by a tungsten filament (12 – 14 amps) to induce the decomposition of the hydrocarbons [3]. The key steps in this fabrication process are described below.

a. For 28 minutes, the furnace temperature was increased from 25 to 750 °C with Ar gas flow (400 sccm).

b. Next, the temperature was maintained at 750 °C for 10 minutes while H_2 (100 sccm) and Ar (400 sccm) were injected. During this process, the Fe layer changed form to Fe nanoparticles.

c. C_2H_4 (147 sccm), H_2 (100 sccm) and Ar (400 sccm) were introduced into the furnace at 750 °C and 1 atm. To grow 22 nm-diameter MWNT, bubbling water (50 sccm) was injected for 1 minute every 15 minutes or continuously to decrease amorphous carbon production and increase the straightness of MWNT [1]. For 13 nm-diameter MWNT, water was not injected. As shown in Fig. S1a, SEM confirmed that the final

lengths of MWNT were similar and that pulsed water injection resulted in well aligned VAMWNT. Figure S2 shows the comparison between 22 nm-diameter MWNT and 13 nm-diameter MWNT. The method for growing 13 nm-diameter MWNT has a lower degree of alignment and a higher quantity of amorphous carbon compared to the 22 nm sample.

d. At the end of the CVD process, the Ar flow rate was decreased to 50−100 sccm in order to weaken bonding between the MWNT array and substrate [4] and create a free-standing aligned MWNT array.

The resulting films were 3 to 5 mm tall on a silicon wafer approximately 5x5 mm in cross-section (Fig. S1a). The MWNT were either dispersed as individual nanotubes for characterization or kept in an array form for further reaction testing. We calculated the porosity of the VAMWNT using a previously published protocol [5]. The mass and volume of the VAMWNT were measured directly. The information about tube diameter and number of walls was obtained from TEM images (Fig. 1b). The 22 nm-MWNT had an average of ten walls, an inner radius of 7.6 nm, and an outer radius of 11 nm, giving them a cross-sectional area of 197.6 nm^2. The porosity was estimated as 99%. Alternative growth conditions (Furnace tube diameter: 29mm, Fe: 0.5 nm, Al_2O_3: 20nm, C_2H_4: 30 sccm, H_2: 55 sccm, Ar: 150 sccm) produced 13 nm-diameter MWNT with an average of nine walls. TEM images are shown in Fig. S1b. The inner radius was 3.4 nm and outer radius was 6.5 nm. The cross-sectional area was 96.4 nm^2 and the porosity was 97%.

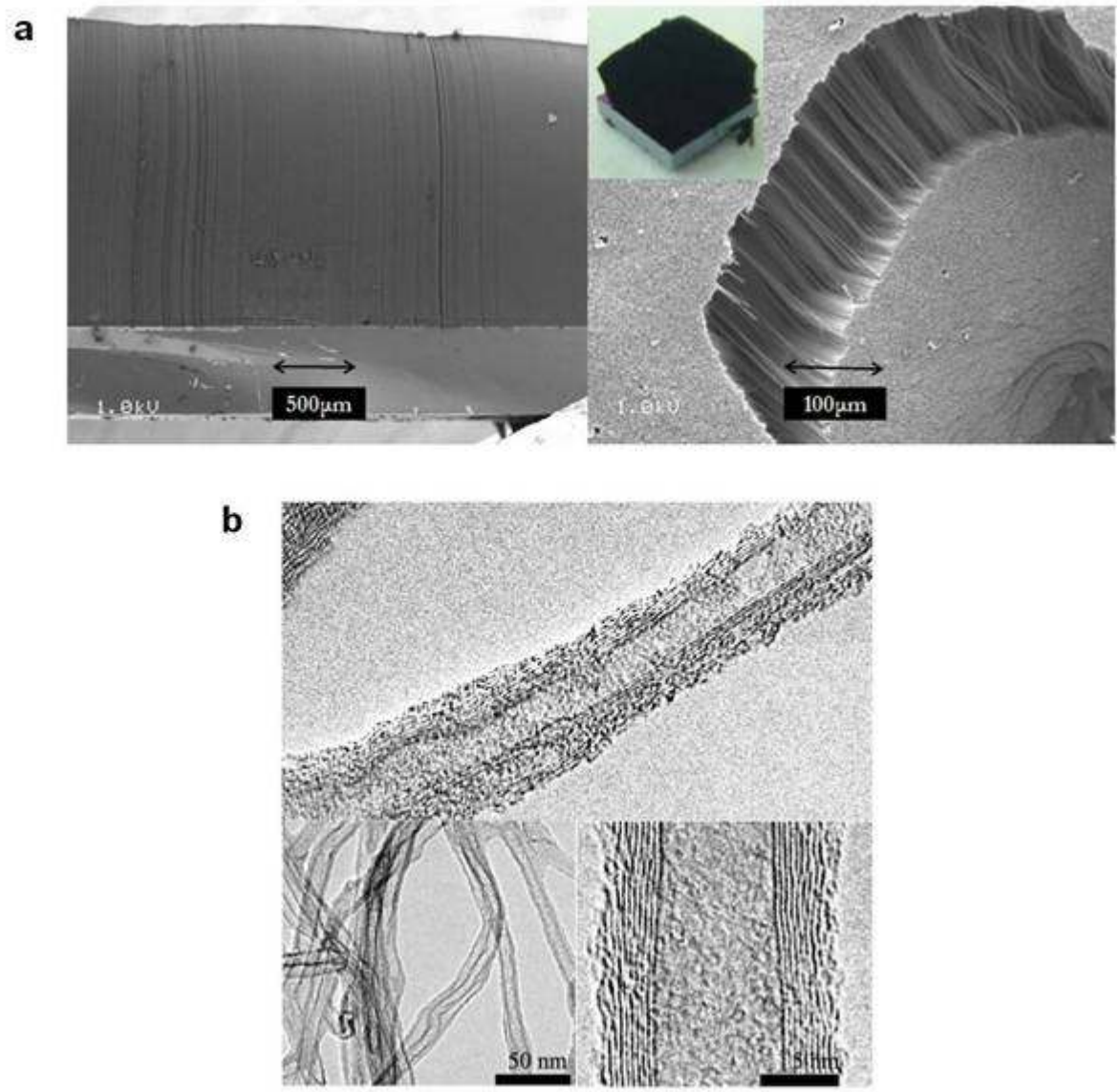

Figure S1 | Microscopic images of VAMWNT. a, Scanning electron microscopic images of nanotubes synthesized using water injection method. Cross-section is 5 **x** 5 mm and average height is 3 to 5 mm. **b,** Transmission microscopic images. Inner diameter is 7 to 8 nm, and outer diameter is 11 to 13 nm.

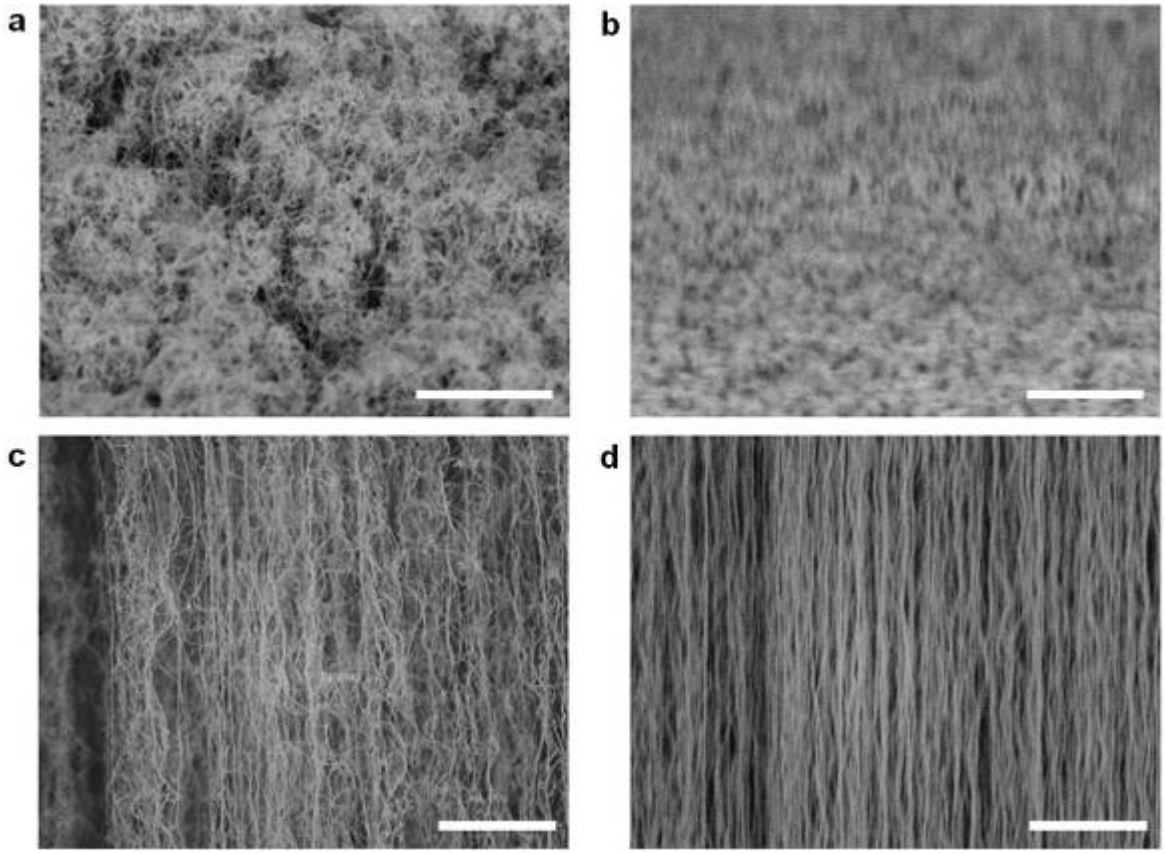

Figure S2 | Scanning electron microscope images of VAMWNT with (22 nm-diameter MWNT) or without water-assisted method (13 nm-diameter MWNT). a, Tilted view of VAMWNT without water-assisted method. A great deal of amorphous carbon exists on the top surface. **b,** Tilted view of VAMWNT with water-assisted method. The top surface of the VAMWNT is clear. **c,** Side view of VAMWNT without water-assisted method. The array is relatively poorly aligned. **d,** Side view of VAMWNT with water-assisted method. The array is relatively well aligned. All scale bars indicate 1 μm.

2. Synthesis and characterization of TNA-MWNT

TNA was received in a sand mixture. Washing the mixture with acetonitrile dissolved TNA. The solution was filtered to eliminate impurities, resulting in pure TNA solution. 0.2 g of TNA was dissolved in 10 mL of acetonitrile. The solution was added to VAMWNT. When liquids are introduced into sparse VAMWNT and evaporated, the cross-section of VAMWNT significantly shrinks due to the surface tension of the liquid and strong van der Waals interactions between nanotubes [6]. Thus TNA was trapped among the MWNT and coated their walls (Fig. 1b). The aligned structure of TNA-MWNT was maintained after the wet impregnation as shown in Fig. S3a. The TNA shows up as a bright coating compared to the nanotubes (Fig. S3b). 5 μL of NaN_3 in aqueous solution with a concentration of 50 mg/mL was then added to serve as a primary igniter, since NaN_3 has a much lower activation energy (40 kJ/mol) [7] than TNA (120–200 kJ/mol) [8]. The VAMWNT were dried under atmospheric conditions (300 K, 1 atm) for 24 hours.

The mass of the array was measured with a microbalance before and after impregnation to determine the mass ratio of TNA to MWNT. The mass ratio could be controlled by the concentration and amount of TNA solution added to the VAMWNT. Figure S4 shows the X-ray diffraction data demonstrating that both the crystal structures of MWNT and TNA are preserved in the composite.

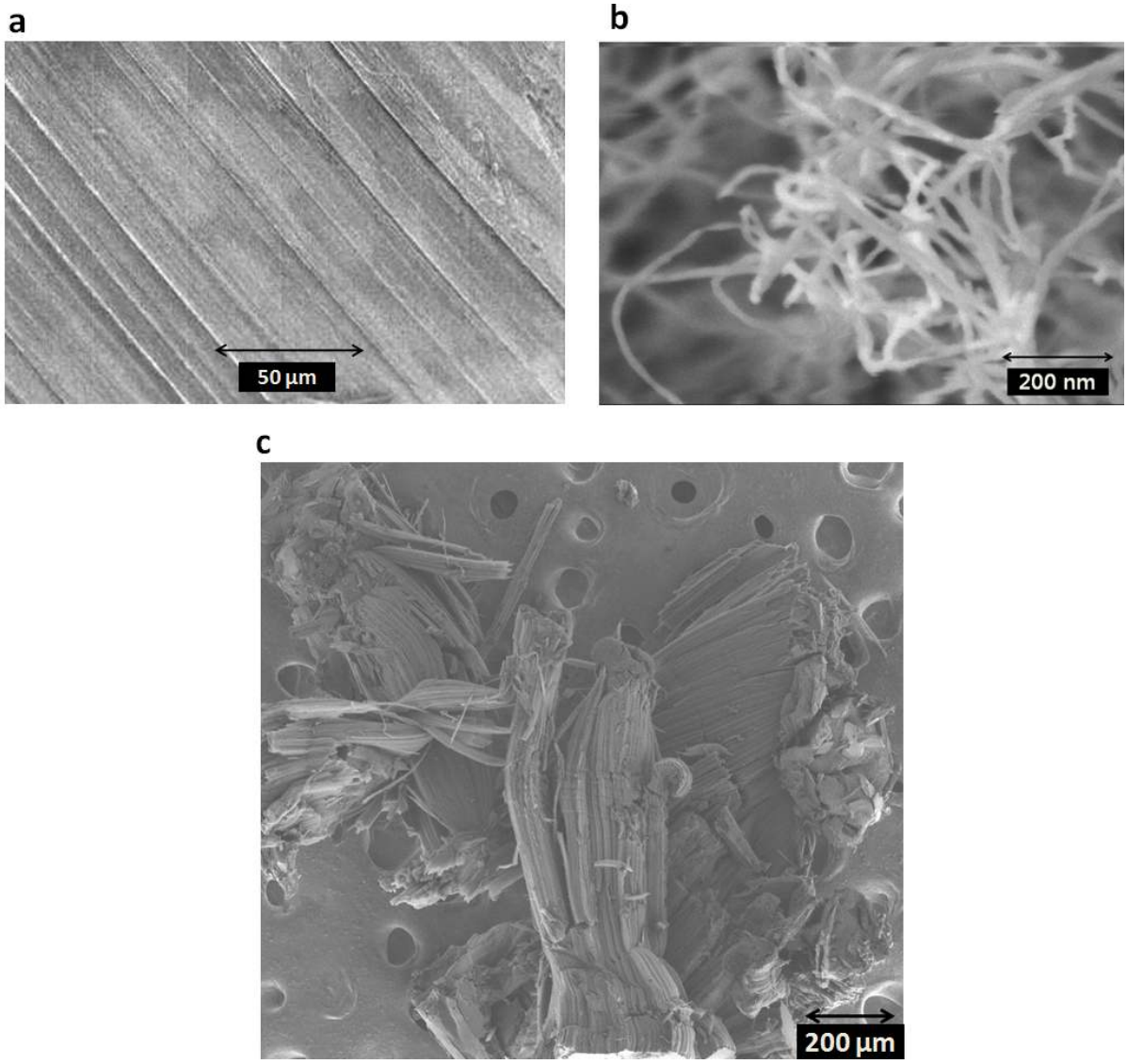

Figure S3 | TNA-MWNT scanning electron microscopic images. Each TNA-coated MWNT was dispersed from the bundles before electron microscopy. **a,** The aligned structure was maintained after the wet impregnation. In several places, larger crystallites of TNA were visible, as in the transmission electron microscopic images of Fig. 1b. **b,** The TNA shows up as a bright coating compared to the nanotubes. **c,** Bulk TNA-MWNT arrays were aligned along length axis, and were

more densely packed in comparison with MWNT arrays lacking TNA due to capillary forces during evaporation.

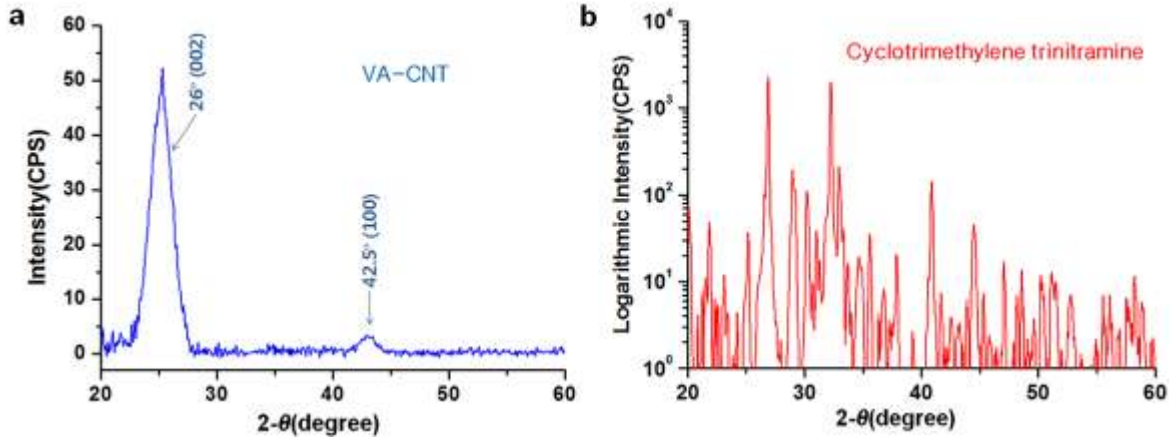

Figure S4 | X-ray diffraction patterns of VAMWNT and TNA before synthesis

a, VAMWNT have two peaks. 26° (002) corresponds to the inter-tube spacing of 0.34 nm and 42.4° (100) to 2.12 nm crystal spacing [9-11]. The (002) plane peak depends on the alignment of the MWNT; the peak will shift away from 26° with decreasing degree of alignment. **b,** TNA has many XRD peaks since it has numerous crystal polymorphs.

3. Reaction Velocity Measurements

Ignition methods

Either laser irradiation (785 nm, 300 to 400 mW) or high voltage electrical discharge (up to 2.8 kV, 5 mA) was used to ignite samples (Fig. S5, Fig. S6). For the high voltage electrical discharge, a thin tungsten wire was fixed to the TNA-MWNT, keeping a small gap between them and the tungsten

plate below (Fig. S6a). The two tungsten elements served as electrodes for the sub-ms high voltage discharge.

Reaction velocity measurement

An optical fiber array was used to measure reaction velocity. This system can detect light emission from a small reaction region at high speed. The TNA-MWNTs were attached to a metallic fixture with a temperature control apparatus. TNA-MWNT were preheated on the fixture and ignited with a 785 nm, 400 mW laser pulse. Figure S5 shows a schematic of setup and signals acquired from two optical fibers. The data used to generate Fig. 2b are summarized in Table S1. Alternative measurement method was high speed photography. A high speed CCD camera (CPL-MS70K, Canadian Photonic Labs) with a microscopic lens (Macro 60 mm, f/2.8D micro Nikkor Autofocus lens, Nikon) recorded the reaction at 90,000 frames per second (Fig. S6). Another method to extract reaction front velocity used thermopower voltage signals (Fig. S7, S8). The thermopower voltage signal contains information about reaction propagation over the whole sample volume. It can be divided into two regions (Fig. S8): a strong oscillation region and smooth region. There is a significant body of literature on velocity oscillation in traditional combustion waves[12,13], and most samples exhibited an oscillation region initially. Comparison between optical microscopy and the electrical signal shows that this region appears to coincide with the self-propagating wave front. There is good agreement between the initial rise time of the thermally induced voltage signal and the optically measured reaction front. The smooth zone appears to be thermoelectric voltage generation due to the residual temperature gradient following the rapidly propagating wave. The reaction velocities determined from thermopower voltage signals appear in Fig. S9. One reason for the scaling of reaction velocity in Fig. S9 is orthogonal heat transfer in the TNA-MWNT

arrays. Figure S9b explains the 2-dimensional flame dissipation in larger samples. Figure S7 is the histogram of compiled data sets measured by all 3 methods.

Control experiments

We investigated the effect of thickness of TNA on reaction velocity. There were optimal mass ratios of TNA to MWNT, which varied based on total sample mass that maximized reaction velocity. A very thin TNA layer cannot supply enough heat from its exothermic reaction to aid reaction propagation, although the unreacted region of TNA requires small total amount of energy for reaction. On the contrary, when TNA layer is very thick, the exothermic reaction can provide more heat energy, but the unreacted region needs large amounts of energy for reaction. Consequently, we might expect that there is an optimal ratio to promote fast reaction velocities.

Also, we designed experiments to understand the role of aligned CNTs in chemical reactions in TNA-MWNT arrays. TNA composites were made with porous activated carbon (AC) with a large surface area and unaligned CNTs (Length: 500 nm - 1.5 μm) by means of the same wet impregnation method. TNA-AC needed much more energy to initiate reaction, and its reaction velocity was slower than that of a TNA-MWNT array. Although TNA-unaligned CNTs required similar initiation energy to TNA-MWNT, the reaction velocity was still slow, and this composite could not sustain a continuous reaction. During the reaction, part of the TNA-unaligned CNTs was separated by a pressure wave from the exothermic reaction. We conclude that CNTs' one-dimensional structure and high axial thermal conductivity contribute to enhancing the reaction velocity dramatically. Also, the structure of the MWNT array helps to shape the TNA coating layer around the CNT walls continuously, thus maintaining reaction propagation. Finally, CNTs decrease the initiation energy of the reaction enormously compared to TNA-AC.

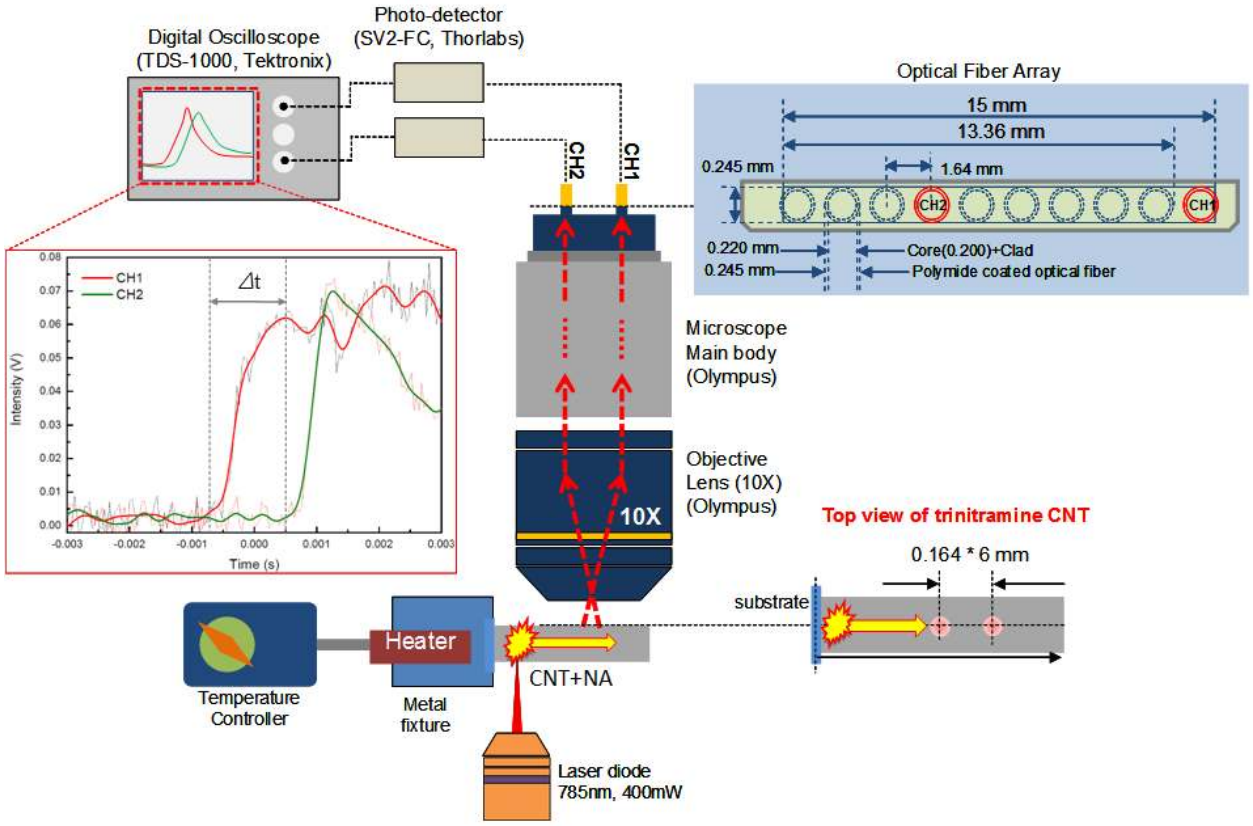

Figure S5 | Reaction velocity measurements using an optical fiber array with microscopic lens system. Reaction propagation was monitored using optical fibers connected to a microscope. A photo-detector (SV2-FC, Thorlabs, rise and fall time < 150 ps) converted optical signals into electrical signals, which were then digitized with an oscilloscope (TDS-1000, Tektronix, 1 GS/s). The time delay between the two channel signals (CH1 and CH2) was used to calculate reaction velocity. The distance between the two channel spots on the surface of the sample was 984 μm. The optical fiber array was aligned along the length axis of the VAMWNT to measure the parallel reaction velocity. For an orthogonal reaction velocity measurement, the fiber array was rotated by 90 degrees.

Orientation	Temp. (°C)	Specimens	Time delay between two signals (s)	Reaction velocity (m/s)	Avg.velocity (m/s)	Std. Dev. (m/s)
Parallel	25	PA-25-1	0.00776	0.127	0.130	0.003
		PA-25-2	0.00736	0.134		
		PA-25-3	0.00752	0.131		
	60	PA-60-1	0.00392	0.251	0.205	0.041
		PA-60-2	0.00512	0.192		
		PA-60-3	0.00576	0.171		
	100	PA-100-1	0.00408	0.241	0.297	0.165
		PA-100-2	0.00588	0.167		
		PA-100-3	0.00204	0.482		
	130	PA-130-1	0.00244	0.403	0.353	0.119
		PA-130-2	0.00212	0.464		
		PA-130-3	0.00276	0.357		
		PA-130-4	0.00528	0.186		
	180	PA-180-1	0.00156	0.631	0.755	0.143
		PA-180-2	0.00108	0.911		
		PA-180-3	0.00136	0.724		
Perpendicular	25	PE-25-1	0.01300	0.076	0.066	0.011
		PE-25-2	0.01476	0.067		
		PE-25-3	0.01812	0.054		
	60	PE-60-1	0.01700	0.058	0.059	0.002
		PE-60-2	0.01612	0.061		
		PE-60-3	0.01708	0.058		
	100	PE-100-1	0.01572	0.063	0.067	0.017
		PE-100-2	0.01144	0.086		
		PE-100-3	0.01896	0.052		
	130	PE-130-1	0.00764	0.129	0.147	0.018
		PE-130-2	0.00600	0.164		
		PE-130-3	0.00664	0.148		
	180	PE-180-1	0.00500	0.197	0.174	0.046
		PE-180-2	0.00816	0.121		
		PE-180-3	0.00484	0.203		

Table S1 | Data used in Fig. 2b.

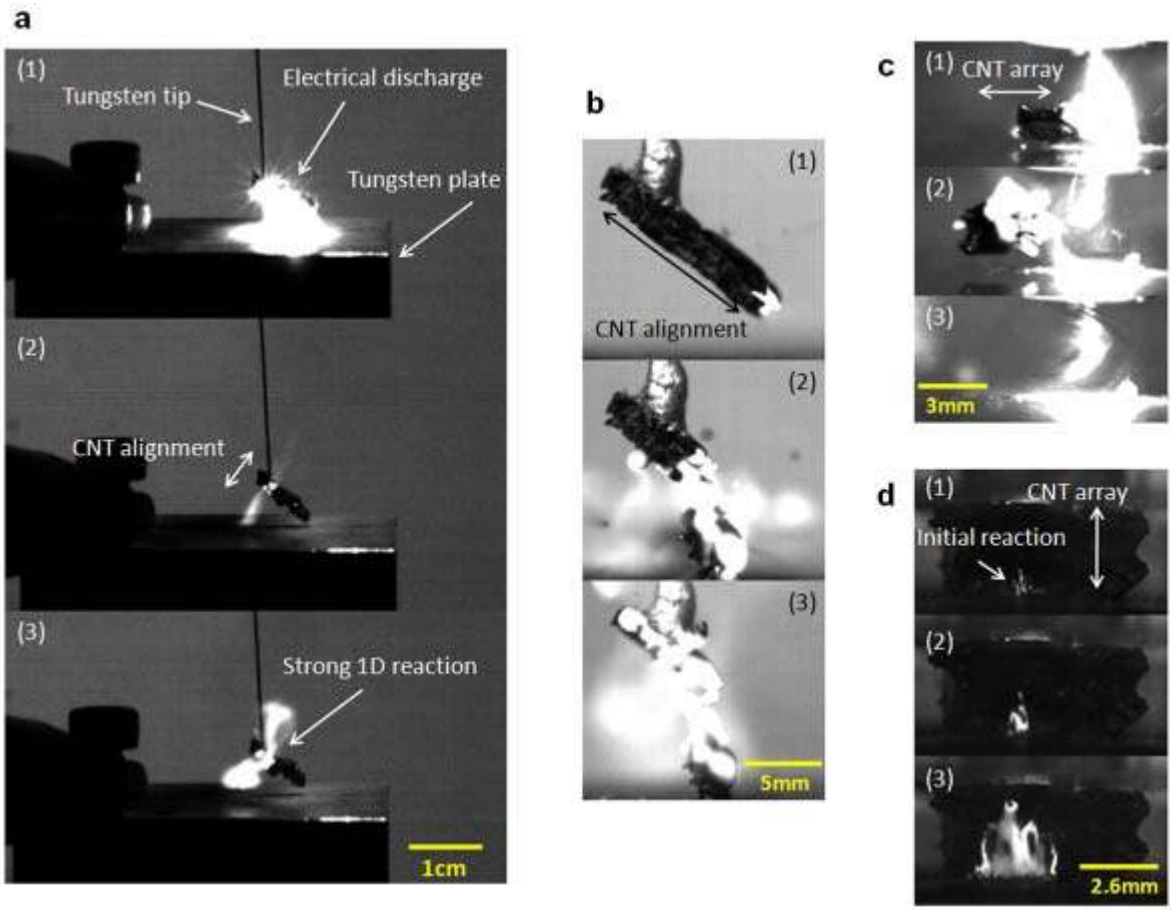

Figure S6 | High speed photographic images. a, TNA-MWNT were attached to a thin tungsten wire. A tungsten plate was placed below the sample, leaving a small gap. A high voltage power supply (up to 2.8 kV, 5 mA) was connected to the tungsten wire and the plate. This produced an electrical discharge between the TNA-MWNT and the tungsten plate that ignited the reaction. **b,** The reaction front velocity was measured from magnified high speed photographic images. **c,** Launching TNA-MWNT in the direction of their alignment for free body experiment. A laser (785nm, 340 mW) ignited the sample on the top surface. Thrust force in the direction of alignment of the MWNT was generated, which launched the sample towards the left of the image. **d,** Flame propagation in TNA-MWNT bulk array. An electrical discharge ignited the sample at its base. The

reaction propagated in the direction of nanotube alignment initially (images 1 and 2), but eventually spread outward in the radial direction.

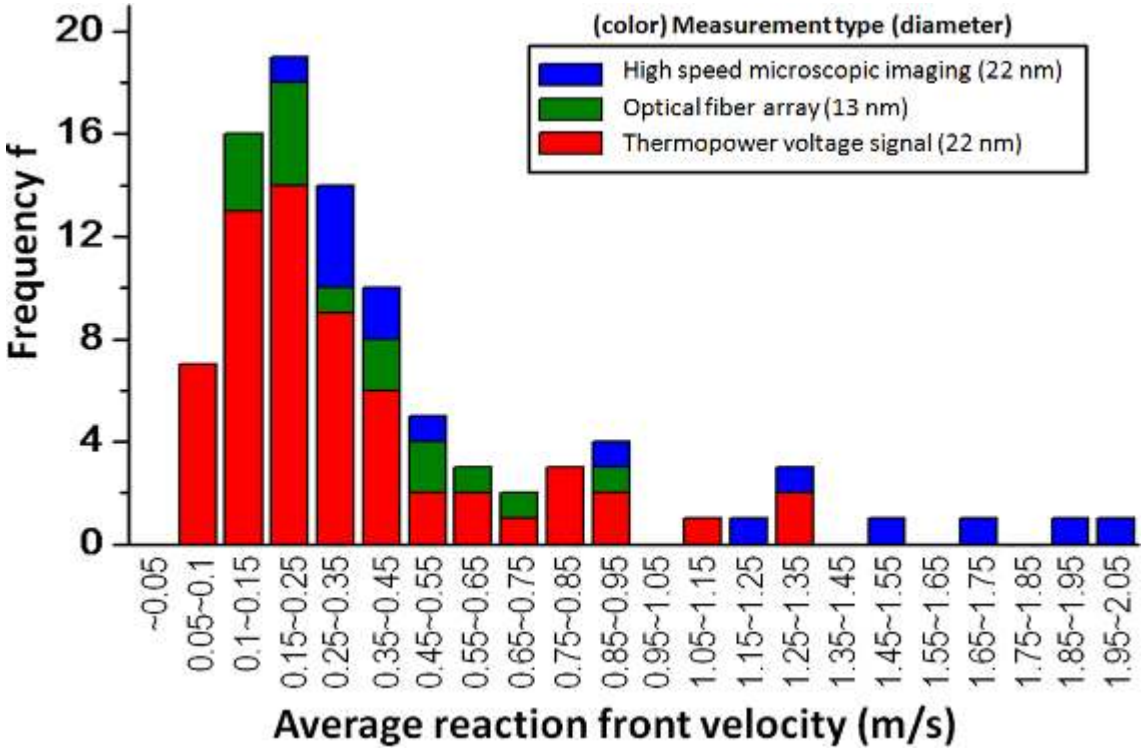

Figure S7 | Histogram of compiled data sets of TNA-MWNT reaction velocity. This histogram includes results from three different reaction velocity measurement techniques. High speed microscopic imaging or optical fiber array can capture multiple positions of the wave front in time, yielding an accurate velocity. Also, the initial transient rise of the thermopower voltage correlates with the reaction front velocity.

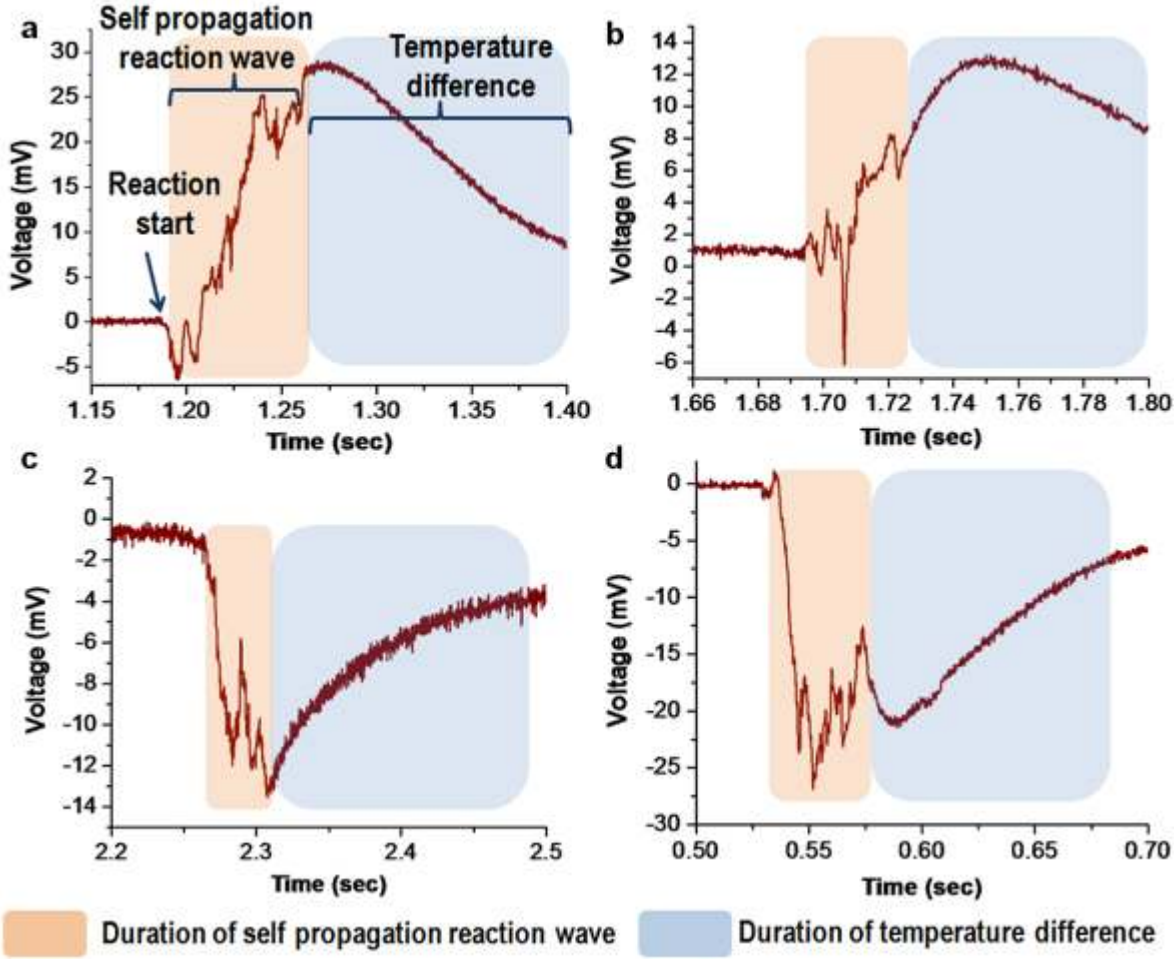

Figure S8 | Thermopower voltage signal in reaction zone and cooling zone. The thermopower voltage signal is divided into two regions. Initial transient oscillation zone indicates reaction time[12,13], and smooth zone reflects cooling time. **a, b,** Positive voltage generation with clear oscillation and smooth regions. **c, d,** Negative voltage generation with oscillation and smooth zones.

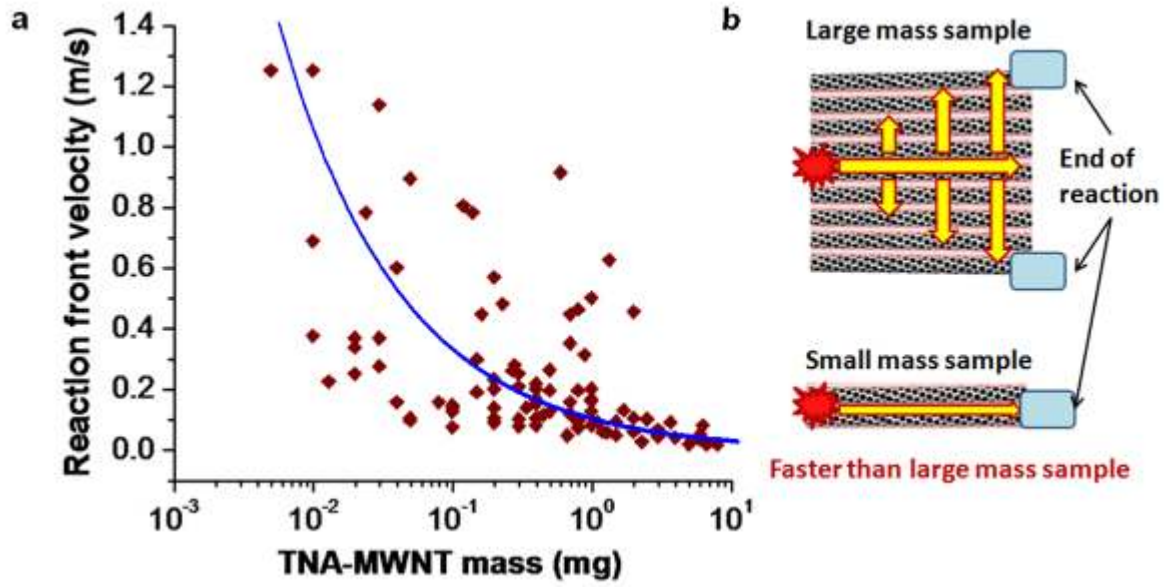

Figure S9 | Reaction front velocity calculated from thermopower voltage signal. a, TNA-MWNT reaction velocity plotted as a function of total mass of TNA-MWNT. The blue line is a curve fit of reaction velocity based on TNA-MWNT total mass. **b,** Illustration of differences in reaction propagation between small mass (1D) and large mass (2D) TNA-MWNT samples.

4. Modeling of Reaction Propagation with Convection and Radiation

To model a coupled TNA-MWNT system, we begin with a standard one-dimensional heat balance for the TNA, including terms for heat conduction, reaction, and coupling with the nanotube.

$$\frac{\rho C_p}{M_W}\frac{\partial T}{\partial t} = \chi\frac{\partial^2 T}{\partial x^2} - (Qk_o y)Exp\left(-\frac{E_a}{RT}\right) - G_1(T - T_2) - \frac{hS}{V}(T - T_{atm}) - \frac{\varepsilon\sigma S}{V}(T^4 - T_{atm}{}^4)$$

where $G_1 = G_0\dfrac{4d_N}{d_M{}^2 - d_N^2}$.

Variables with no subscript refer to TNA, subscript "2" refers to the nanotube, T is temperature, t is time, x is distance, χ is thermal conductivity, ρ is density, Q is the enthalpy of combustion, C_p is the (molar) specific heat, M_W is molecular weight, y is the molar concentration of TNA , k_0 is the Arrhenius prefactor, R is the universal gas constant, and E_a is the activation energy, h is convective heat transfer coefficient, S/V is surface area to volume ratio for TNA configuration, ε is the emissivity, σ is the Stephan-Boltzmann constant, T_{amb} is the temperature of the surroundings, d_M is the total diameter of the TNA-MWNT system, d_N is the nanotube diameter, and G_0 is the interfacial conductance. The aspect ratio of the TNA-MWNT system is large enough that other spatial dimensions are unimportant. Phase changes can be neglected by using material parameters averaged over multiple phases.

Likewise, we can write a heat balance for the nanotube

$$\frac{\rho_2 C_{p,2}}{M_{W2}}\frac{\partial T_2}{\partial t} = \chi_2 \frac{\partial^2 T_2}{\partial x^2} + G_2\left(T - T_2\right)$$

where $G_2 = G_0 \dfrac{4}{d_N}$. Reaction and phase changes in the nanotube can be neglected since MWNT are thermally stable up to very high temperatures, even above 2000 K. Furthermore, if the nanotube does break down, it will be after the reaction front passes, so the breakdown will have little effect on the velocity of the reaction front.

We define the reaction kinetics as first-order in TNA:

$$\frac{\partial y}{\partial t} = -k_o\, y Exp\left(-\frac{E_a}{RT}\right)$$

Now we non-dimensionalize temperature, time, distance, and TNA concentration using reaction and thermal parameters to simplify the numerical calculations.

$$u = \left(\frac{R}{E_a} \right) T$$

$$u_2 = \left(\frac{R}{E_a} \right) T_2$$

$$\tau = \left(\frac{-Qk_o R}{C_p E_a} \right) t$$

$$\xi = x \sqrt{\left(\frac{\rho C_p}{\chi M_W} \right) \left(\frac{-Qk_o R}{C_p E_a} \right)}$$

$$\frac{M_W y}{\rho} = 1 - \eta$$

η is the extent of conversion.

Now it is helpful to define

$$\beta = \frac{C_p E_a}{-QR}$$

and thermal diffusivity for each material, α and α_2, in the form

$$\alpha = \frac{\chi M_W}{\rho C_p}$$

With these substitutions, the equations become

$$\frac{\partial u}{\partial \tau} = \frac{\partial^2 u}{\partial \xi^2} + (1 - \eta) e^{-1/u} - \gamma_1 (u - u_2) - l(u - u_{atm}) - w(u^4 - u_{atm}{}^4)$$

$$\frac{\partial u_2}{\partial \tau} = \alpha_0 \frac{\partial^2 u_2}{\partial \xi^2} + \gamma_2 (u - u_2)$$

$$\frac{\partial \eta}{\partial \tau} = \beta (1 - \eta) e^{-1/u}$$

where $\alpha_0 = \frac{\alpha_2}{\alpha}$, $\gamma_1 = \frac{G_1 \beta M_W}{\rho C_p k_0}$, $\gamma_2 = \frac{G_2 \beta M_{W2}}{\rho_2 C_{p,2} k_0}$, $l = \frac{hSM_W \beta}{V \rho k_0 C_p}$, and $w = \frac{\varepsilon \sigma S M_W \beta}{V \rho k_0 C_p}$

We then set initial boundary equations as follows, igniting the left end of the system to launch steady thermal wave propagation by means of a Gaussian temperature pulse[12].

τ = 0: u = Gaussian temperature pulse centered on ξ =0

τ = 0, $\xi \geq 0$: u_2 = 0.012425 (298 K)

τ = 0, ξ >0: u = 0.012425 (298 K)

τ = 0, ξ > 0: η = 0

τ = 0, ξ = 0: η = 0.999

To solve the equations, we assume maximum thermal diffusivity of CNT, α (10^{-5} to 10^{-2}), and β (5 to 35) are varied as parameters for our contour plot (Fig. 2c). We assume several material properties are constant on the basis of previous literature sources[14-23]. The molecular weight of TNA is 0.22212 kg/mol, its thermal conductivity [14] is 0.2783 W/m/K, and its density[15] is 1820 kg/m^3. The activation energy for decomposition of TNA is 127 kJ/mol [8]., and k_0 is 3.75 x 10^{18} s^{-1}. To simulate the TNA-MWNT system more accurately, we used temperature-dependent properties of TNA (Table S2) and CNT (Table S3). The reaction front velocity is thus calculated as 1.3 m/s (Fig. S10), very similar to the experimental results. Also, we investigated the effect of convection and

radiation. The dimensionless heat convection coefficient, *l,* and dimensionless radiation coefficient, *w,* depend on k_0. As k_0 decreased, the reaction front velocity decreased (Fig. S11). But within the normal range of TNA [16] parameter values, convection and radiation did not affect the results.

TNA Basic properties	Cp (J/mol/K)	Q (kJ/mol)	α (m^2/s)	β
Temperature (Kelvin)	**Specific heat**	**Heat of combustion**	**alpha**	**Beta**
300	239.56	876.00	1.42E-07	4.18
400	317.90	874.98	1.07E-07	5.55
500	396.25	881.24	8.57E-08	6.87
600	474.59	894.68	7.16E-08	8.10
700	552.94	915.23	6.14E-08	9.23
800	631.29	942.85	5.38E-08	10.23
900	709.63	977.56	4.79E-08	11.09
1000	787.98	1019.40	4.31E-08	11.81
1100	866.32	1068.41	3.92E-08	12.39
1200	944.67	1124.64	3.60E-08	12.83
1300	1023.02	1188.14	3.32E-08	13.15
1400	1101.36	1258.97	3.08E-08	13.36
1500	1179.71	1337.16	2.88E-08	13.48
1600	1258.06	1422.76	2.70E-08	13.51
1700	1336.40	1515.81	2.54E-08	13.47
1800	1414.75	1616.35	2.40E-08	13.37
1900	1493.09	1724.42	2.27E-08	13.23
2000	1571.44	1840.04	2.16E-08	13.05
2100	1649.79	1963.14	2.06E-08	12.84
2200	1728.13	2094.01	1.97E-08	12.61
2300	1806.48	2232.22	1.88E-08	12.36
2400	1884.82	2378.36	1.80E-08	12.11
2500	1963.17	2532.03	1.73E-08	11.84
2600	2041.52	2693.45	1.66E-08	11.58
2700	2119.86	2862.39	1.60E-08	11.31
2800	2198.21	3039.15	1.55E-08	11.05
2900	2276.55	3223.46	1.49E-08	10.79
3000	2354.90	3415.59	1.44E-08	10.53

Table S2 | Temperature-dependent thermal properties of TNA [14,16-19]

MWNT Basic properties	Cp(J/mol/K)	k (W/m-K)	α (m^2/s)
Temperature (Kelvin)	Specific heat	Thermal conductivity	alpha
300	7.8	2347	0.002786
400	10.3	2686.96	0.002415
500	12.8	3000	0.002170
600	15.1	1956	0.001199
700	17	1695	0.000923
800	18.1	1435	0.000734
900	19	1304.35	0.000636
1000	19.8	1148	0.000537
1100	20.5	1017.4	0.000460
1200	21	913.045	0.000403
1300	21.4	834.8	0.000361
1400	21.7	756.2	0.000323
1500	22	717.4	0.000302
1600	22.2	678.3	0.000283
1700	22.4	620	0.000256
1800	22.6	563.91	0.000231
1900	22.8	547	0.000222
2000	23	535	0.000215
2100	23.1	520	0.000208
2200	23.2	508	0.000203
2300	23.3	497	0.000198
2400	23.4	487	0.000193
2500	23.5	478	0.000188
2600	23.6	470	0.000184
2700	23.6	463	0.000182
2800	23.7	457	0.000179
2900	23.7	452	0.000177
3000	23.7	450	0.000176

Table S3 | Temperature-dependent thermal properties of MWNT [20-23]

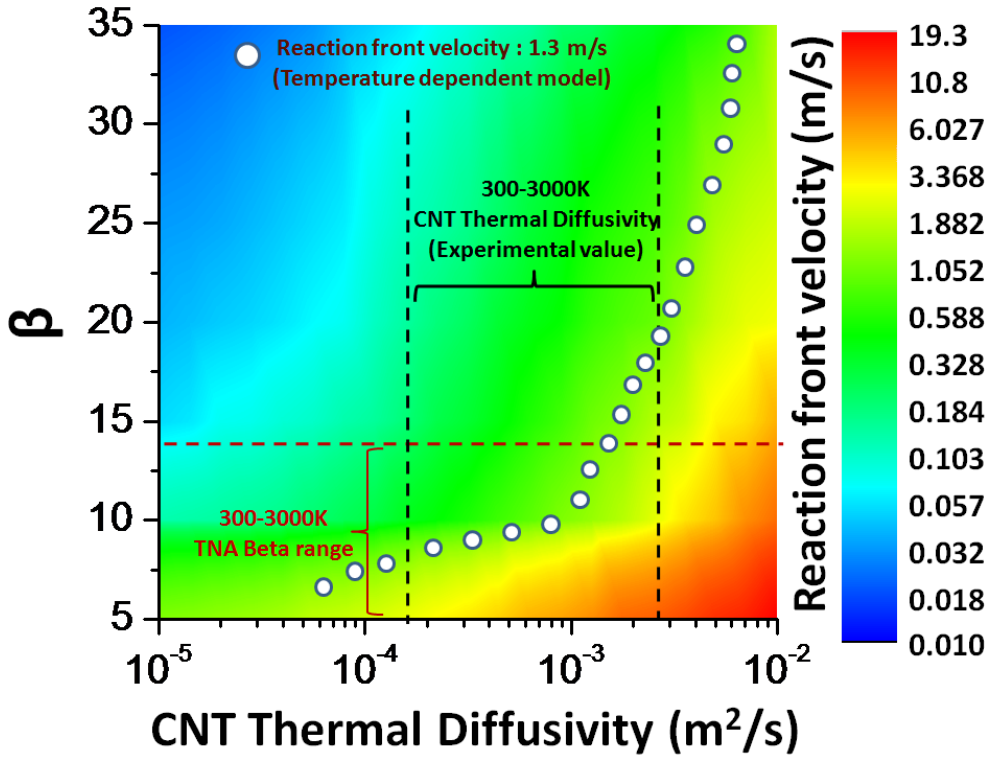

Figure S10 | Reaction front velocity using temperature-dependent thermal properties for TNA and CNT. The reaction front velocity is 1.3 m/s. β and thermal diffusivity values are from other literature sources [14]. β is in the range of 4.2 to 13.5 (Table S2), and CNT thermal diffusivity (Table S3) is in the range of 0.0002 to 0.002.

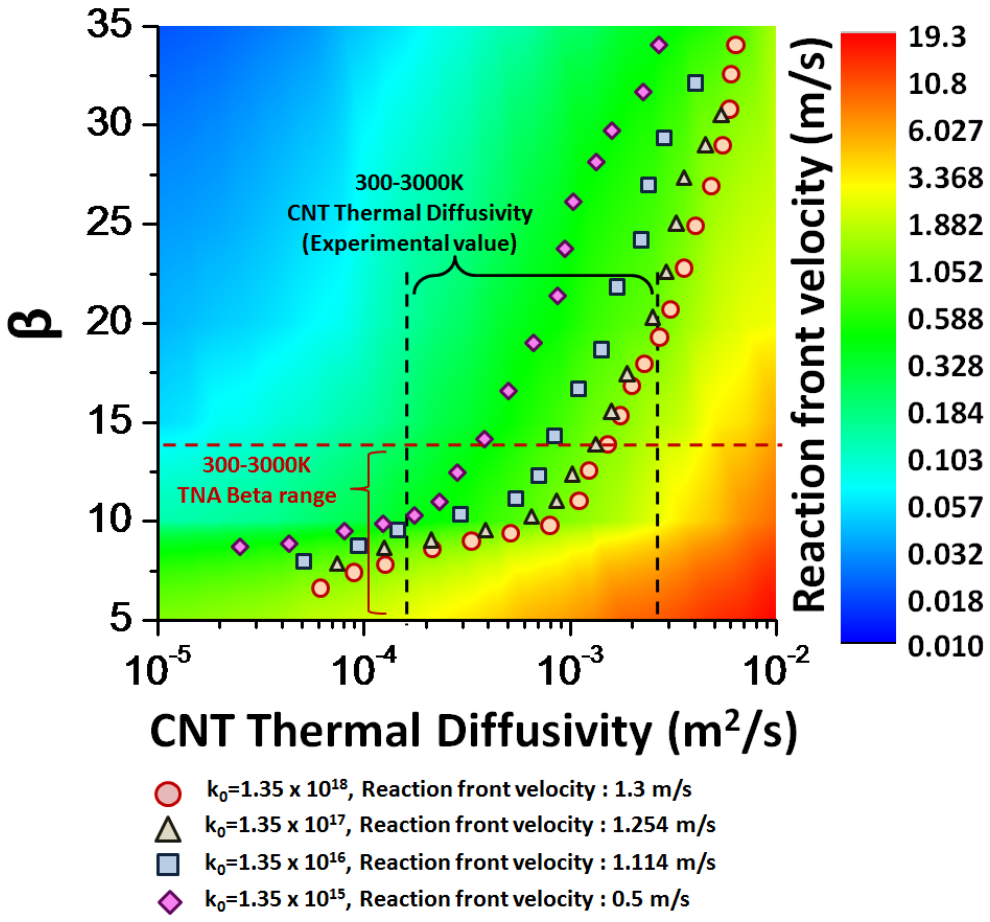

Figure S11 | Reaction front velocity using temperature-dependent thermal properties for TNA and CNT, as well as convection and radiation. The reaction front velocity is 1.3 m/s at $k_0 = 3x10^{18}$ (s^{-1}), the same as our thermal wave propagation model without convection and radiation. A decrease in the reaction rate constant results in a decrease in reaction velocity.

After steady state wave propagation is attained, the reaction front velocity is constant along the whole MWNT. A dimensionless distance ξ = 1000 was sufficient to simulate steady state reaction front velocity. The non-dimensionalized distance of MWNT length 2.36 mm is many orders of magnitude larger than ξ = 1000. Thus, for lengths above 1000, the reaction front velocity will be constant.

Interfacial thermal conductivity, *G*, between TNA and MWNT should not be the limiting factor in reaction front velocity enhancement [24], and we confirmed this for this model (Fig. S12). In the case of low thermal resistance between TNA and MWNT, rapid thermal equilibrium is achieved on the boundary between the two materials ($u \approx u_2$). Higher interfacial conductance does not affect the temperature profiles of the two materials or the reaction front velocity, as long as the interfacial conductance is over some minimum value. Simulation results indicated that the minimum value of G for these conditions is 9×10^5 W/m^2/K.

We define the location of the reaction front at each point in time as the point where η (the extent of chemical conversion of the reactive annulus) is 0.5 and calculate reaction front velocity accordingly, since the shape of the η profile is perfectly maintained after steady state wave propagation is achieved.

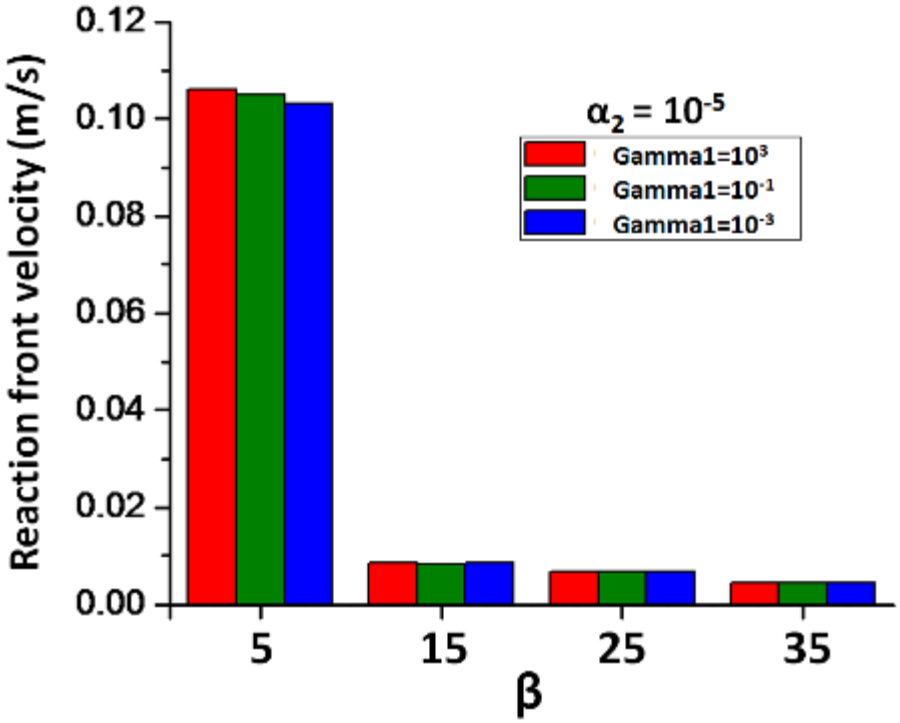

Figure S12 | Effect of interfacial conductance (γ_1) and TNA properties (β) on reaction front velocity. If γ_1 is larger than 10^{-3}, reaction front velocities are approximately the same no matter the value of γ_1. $\gamma_1 = 10^{-3}$ corresponds to $G_0 = 9\text{x}10^5$ W/m^2/K, $\gamma_1 = 10^{-1}$ is $G_0 = 9\text{x}10^7$ W/m^2/K, and $\gamma_1 = 10^3$ is $G_0 = 9\text{x}10^9$ W/m^2/K. Velocities shown here are the same as Fig. 2c for the $\alpha_2 = 10^{-5}$ m^2/s case.

5. Modeling of thermopower depending on TNA-MWNT mass

$$\frac{P}{M_t} = \frac{S^2}{R_i \rho \pi r^2 L} \int_0^L \frac{dT}{dL} dL$$

$$T_N = \exp\left(-\frac{kA}{\rho C_P V} \frac{L}{v} \right) (T_H - T_L) + T_L$$

where P is thermopower, M_t is the mass of TNA-MWNT, S is the Seebeck coefficient of nanotubes, R_i is electrical resistance, ρ is the density of nanotubes, r is the radius of nanotubes, L is the length of the region that the thermal wave propagates, T is temperature (spatially dependent), T_N is the lowest cooled temperature behind the reaction zone, T_H is the temperature of the reaction front, T_L is the ambient temperature, C_p is the specific heat of nanotubes, V is the volume of nanotubes, A is the area in contact with cooling source, k is the coefficient of all cooling effects including thermal contact resistance, convection, radiation, and v is the reaction velocity of thermal wave. Reaction velocities from experimental results were used to fit a curve to the data (Fig. S9). We assume that reaction front temperature T_H is the adiabatic flame temperature. In the case of small mass TNA-MWNT, the reaction velocity is much faster than the time scale of heat diffusion; T_N is nearly the same as T_H. But in the case of large mass TNA-MWNT, the time scale of reaction velocity is similar to the time scale of heat diffusion, and cooling behind the reaction front makes T_N lower than T_H. The temperature gradient between T_N and T_H (the region behind the propagating reaction front) is opposite to the temperature gradient between T_L and T_H (the region ahead of the reaction front), and it causes charge carrier movement and a current in the opposite direction. This trend is stronger with the slow reaction velocities of large mass samples than fast reaction velocities, and specific power has an inverse scaling trend.

6. Propulsive Force Measurement

Force measurement

The propulsive force generated by the 1-D reaction was measured with a piezoresistive sensor (FlexiForce sensor, under 5 μs response time, force range 0 to 4.4 N, Tekscan) (Fig. S13). The sample was mounted on the force sensor on a tungsten plate with a lock-up housing to prevent vibration and other movement. The lock-up housing had a small hole to ignite the sample electrically or with a laser. A function generator supplied the electrical signal to the force sensor, and the input and output signals were monitored with a digital oscilloscope (DL 1735E, Yokogawa). The resistance of the sensor increased in proportion to the thrust force generated, which was applied perpendicular to the sensor. Temperature effects were negligible during the short observation period.

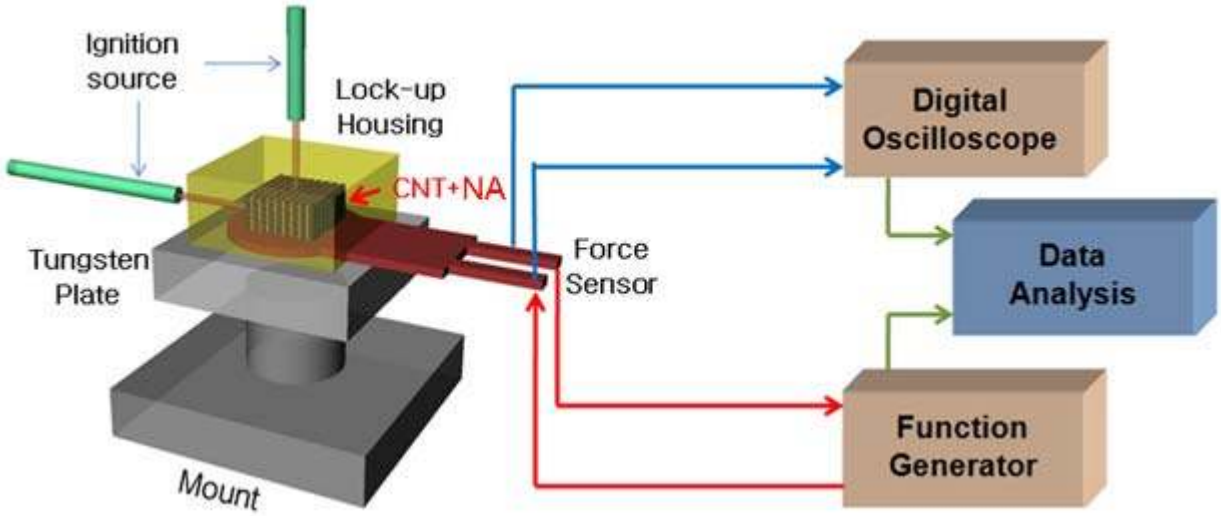

Figure S13 | Schematic illustration of force and impulse measurement of TNA-MWNT. A TNA-MWNT sample was placed normal to the piezoelectric force sensor. A high speed camera simultaneously captured the reaction images.

References

1. Hata, K. et al. Water-assisted highly efficient synthesis of impurity-free single-waited carbon nanotubes. *Science* **306**, 1362-1364 (2004).
2. Xu, Y. Q., Flor, E., Schmidt, H., Smalley, R. E. & Hauge, R. H. Effects of atomic hydrogen and active carbon species in 1 mm vertically aligned single-walled carbon nanotube growth. *Applied Physics Letters* **89**, 123116-123118 (2006).
3. Han, J. H. et al. A mechanochemical model of growth termination in vertical carbon nanotube forests. *Acs Nano* **2**, 53-60 (2008).
4. Liu, K. et al. Controlled termination of the growth of vertically aligned carbon nanotube arrays. *Advanced Materials* **19**, 975-978 (2007).
5. Futaba, D. N. et al. 84% Catalyst activity of water-assisted growth of single walled carbon nanotube forest characterization by a statistical and macroscopic approach. *Journal of Physical Chemistry B* **110**, 8035-8038 (2006).
6. Futaba, D. N. et al. Shape-engineerable and highly densely packed single-walled carbon nanotubes and their application as super-capacitor electrodes. *Nature Materials* **5**, 987-994 (2006).
7. Potvin, H. & Back, M. H. Study of Decomposition of Sodium Azide Using Differential Thermal-Analysis. *Canadian Journal of Chemistry-Revue Canadienne De Chimie* **51**, 183-186 (1973).
8. Williams, M. R. & Matei, M. V. The decomposition of some RDX and HMX based materials in the one-dimensional time to explosion apparatus. Part 1. Time to explosion and apparent activation energy. *Propellants Explosives Pyrotechnics* **31**, 435-441 (2006).
9. Yusa, H. & Watanuki, T. X-ray diffraction of multiwalled carbon nanotube under high pressure: Structural durability on static compression. *Carbon* **43**, 519-523 (2005).
10. Maniwa, Y. et al. Anomaly of X-ray diffraction profile in single-walled carbon nanotubes. *Jpn. J. Appl. Phys., Part 2* **38**, L668-L670 (1999).
11. Cao, A. Y., Xu, C. L., Liang, J., Wu, D. H. & Wei, B. Q. X-ray diffraction characterization on the alignment degree of carbon nanotubes. *Chem. Phys. Lett.* **344**, 13-17 (2001).
12. Weber, R. O., Mercer, G. N., Sidhu, H. S. & Gray, B. F. Combustion waves for gases (Le=1) and solids (L->infinity). *Proceedings of the Royal Society of London Series a-Mathematical Physical and Engineering Sciences* **453**, 1105-1118 (1997).
13. Please, C. P., Liu, F. & McElwain, D. L. S. Condensed phase combustion travelling waves with sequential exothermic or endothermic reactions. *Combustion Theory and Modelling* **7**, 129-143 (2003).
14. Parr, T. & Hanson-Parr, D. RDX ignition flame structure. *Twenty-Seventh Symposium (International) on Combustion, Vols 1 and 2*, 2301-2308 (1998).
15. Li, S. C., Williams, F. A. & Margolis, S. B. Effects of 2-Phase Flow in a Model for Nitramine Deflagration. *Combustion and Flame* **80**, 329-349 (1990).
16. Oyumi, Y. Melt phase decomposition of RDX and two nitrosamine derivatives. *Propell. Explos. Pyrot.* **13**, 42-47 (1988).
17. Liau, Y. C., Kim, E. S. & Yang, V. A comprehensive analysis of laser-induced ignition of RDX monopropellant. *Combust. Flame* **126**, 1680-1698 (2001).
18. Volkov, E. N., Paletsky, A. A. & Korobeinichev, O. P. RDX flame structure at atmospheric pressure. *Combust. Explo. Shock.* **44**, 43-54 (2008).

19. Richard E. Sonntag, G. J. V. w. *Introduction to thermodynamics: classical and statistical* (John Wiley & Sons, 1991).
20. Kim, P., Shi, L., Majumdar, A. & McEuen, P. L. Thermal transport measurements of individual multiwalled nanotubes. *Physical Review Letters* **8721**, 215502-215505 (2001).
21. Begtrup, G. E. et al. Probing nanoscale solids at thermal extremes. *Physical Review Letters* **99**, 155901-155904 (2007).
22. Li, C. Y. & Chou, T. W. Modeling of elastic buckling of carbon nanotubes by molecular structural mechanics approach. *Mechanics of Materials* **36**, 1047-1055 (2004).
23. Li, C. Y. & Chou, T. W. Quantized molecular structural mechanics modeling for studying the specific heat of single-walled carbon nanotubes. *Physical Review B* **71**, 1047-1055 (2005).
24. Abrahamson, J. T., Nair, N. & Strano, M. S. Modelling the increase in anisotropic reaction rates in metal nanoparticle oxidation using carbon nanotubes as thermal conduits. *Nanotechnology* **19**, 195701-195708 (2008).